J. Fluid Mech. (1992), *vol.* 238, *pp.* 1–30
Printed in Great Britain

Three-dimensional dynamics and transition to turbulence in the wake of bluff objects

By GEORGE EM KARNIADAKIS[1]
AND GEORGE S. TRIANTAFYLLOU[2]

[1] Department of Mechanical and Aerospace Engineering and Program in Applied and Computational Mathematics, Princeton University, Princeton, NJ 08544, USA

[2] The Levich Institute and Department of Mechanical Engineering, The City College of New York, New York, NY 10031, USA

(Received 23 April 1990 and in revised form 7 October 1991)

The wakes of bluff objects and in particular of circular cylinders are known to undergo a 'fast' transition, from a laminar two-dimensional state at Reynolds number 200 to a turbulent state at Reynolds number 400. The process has been documented in several experimental investigations, but the underlying physical mechanisms have remained largely unknown so far. In this paper, the transition process is investigated numerically, through direct simulation of the Navier–Stokes equations at representative Reynolds numbers, up to 500. A high-order time-accurate, mixed spectral/spectral element technique is used. It is shown that the wake first becomes three-dimensional, as a result of a secondary instability of the two-dimensional vortex street. This secondary instability appears at a Reynolds number close to 200. For slightly supercritical Reynolds numbers, a harmonic state develops, in which the flow oscillates at its fundamental frequency (Strouhal number) around a spanwise modulated time-average flow. In the near wake the modulation wavelength of the time-average flow is half of the spanwise wavelength of the perturbation flow, consistently with linear instability theory. The vortex filaments have a spanwise wavy shape in the near wake, and form rib-like structures further downstream. At higher Reynolds numbers the three-dimensional flow oscillation undergoes a period-doubling bifurcation, in which the flow alternates between two different states. Phase-space analysis of the flow shows that the basic limit cycle has branched into two connected limit cycles. In physical space the period doubling appears as the shedding of two distinct types of vortex filaments.

Further increases of the Reynolds number result in a cascade of period-doubling bifurcations, which create a chaotic state in the flow at a Reynolds number of about 500. The flow is characterized by broadband power spectra, and the appearance of intermittent phenomena. It is concluded that the wake undergoes transition to turbulence following the period-doubling route.

1. Introduction

The vortex wake of a two-dimensional circular cylinder has become the canonical problem for transition in open flows because, in part, the transition process depends on one parameter only, namely the Reynolds number, Re, of the flow. The transition process in the wake as a function of the Reynolds number can be summarized as follows. At Reynolds number higher than 40 the flow bifurcates to a periodic oscillation, creating a laminar vortex street. Subsequently, the wake undergoes a fast

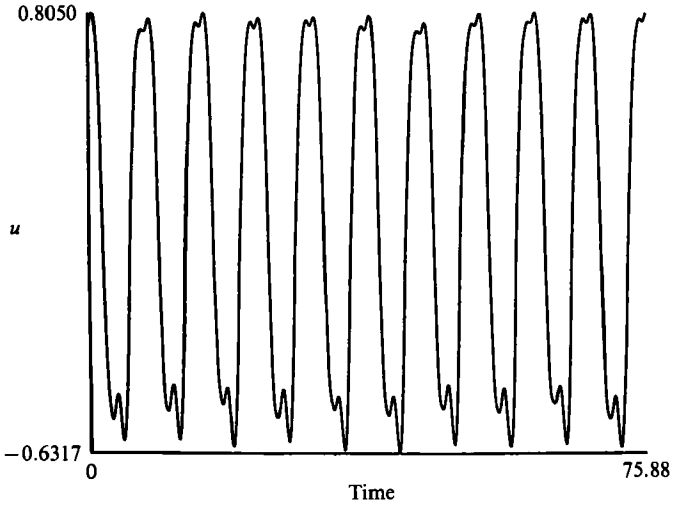

FIGURE 1. Time-history of the streamwise velocity component at point $P_1(x = 2.12; y = 0.45)$ in the near wake ($Re = 500$; two-dimensional simulation).

transition, which starts at Re around 200 and becomes turbulent at Re around 400 (Bloor 1964). No explanation has been offered so far for this transition. The development of computational techniques, as well as of theoretical concepts in hydrodynamic stability and turbulence, offer today the prospect of revisiting this problem and analysing it in much greater detail. The turbulent wake is achieved at relatively low Reynolds number, at which the flow field can accurately be resolved given the presently available computational resources. The main issues here seem to be whether this transition follows some of the universal routes to chaos, and how the universal behaviour is related to the physics of the specific problem.

The first flow bifurcation, which creates the vortex street, can be reliably analysed using two-dimensional simulations, as has been demonstrated by several computational studies in the past (Gresho *et al.* 1984; Karniadakis, Bullister & Patera 1985; Braza, Chassaing & Ha Minh 1986). The applicability of two-dimensional simulations to higher Reynolds number, and more specifically to Reynolds number in the aforementioned transitional regime, seems questionable however, since experiments have reported strongly three-dimensional behaviour after the Reynolds number exceeds a value of about 200 (Williamson 1988). In order to investigate whether any features of the transition process can be captured by two-dimensional simulations, we computed the two-dimensional flow past a circular cylinder at $Re = 500$. A spectral element method has been employed, similar to the one used in Karniadakis & Triantafyllou (1989). A time trace of the streamwise velocity component in the near wake (figure 1) shows that a time-periodic flow state is established. Thus, although the numerical simulation captures the large features of the flow, its results are in qualitative disagreement with experimental observations (Bloor 1964), which, at this Reynolds number, show a 'turbulent' behaviour. This suggests that the transition process is caused entirely by three-dimensionality, and we have to resort to three-dimensional computations to study the transition process. Some corroborating evidence can be found in the experimental work of Hammache & Gharib (1989), who have succeeded in delaying transition in the wake of a circular cylinder through a novel design of end conditions, which suppresses three-dimensional effects.

It appears, however, that independently of end effects, three-dimensionality is an unavoidable state of even nominally two-dimensional wakes, once a certain critical Reynolds number is exceeded. Recent experimental results (Williamson 1988, 1989) place this value around 180, and numerical results (Karniadakis & Triantafyllou 1990) confirm the conclusion. The appearance of three-dimensionality is by itself a fascinating problem and has recently attracted a lot of attention (Meiburg & Lasheras 1988; Lasheras & Meiburg 1990; Williamson 1988, 1989; Hammache & Gharib 1989; Triantafyllou 1990; Kaiktsis, Karniadakis & Orszag 1991), but its connection with the transition to turbulence seems to be the most important reason for studying it. Resolving the issues that are involved here requires the aid of instability theory, vortex dynamics, dynamical systems theory, and the development of reliable and efficient numerical codes based on high-order-accurate schemes for simulating highly unsteady three-dimensional flows. There is certainly a higher degree of complexity involved in three-dimensional flows; strong mixing and chaos, for example, can also be observed in two-dimensional flows, but for *stationary* flows exponential stretching of fluid elements can only occur in three-dimensions (see also Arnol'd 1972).

It is widely recognized that the appearance of a secondary instability is one of the main mechanisms through which a two-dimensional flow becomes three-dimensional. The secondary instabilities operate on two-dimensional waves of finite amplitude, rather than some initial stationary state, and induce an exponential growth rate through the simultaneous action of vortex stretching and tilting. This scenario was suggested by Pierrehumbert & Widnall (1982) for free shear layers, and Orszag & Patera (1983) for several simple-geometry wall-bounded flows. More recently, Pierrehumbert (1986) and Bayly (1986) have proposed that short-wavelength secondary instabilities of inviscid vortices are universal, and constitute the mechanism of energy transfer from large to small scales. Comprehensive reviews of the existing work on secondary instabilities can be found in Bayly, Orszag & Herbert (1988), and Herbert (1988). The presence of secondary instabilities in wall-bounded flows with complex geometry and the existence of stable tertiary states have been demonstrated numerically by Karniadakis & Amon (1987), and Amon & Patera (1989), and more recently by Kaiktsis *et al.* (1991).

The connection, between the secondary instability mechanism and the appearance of three-dimensionality in wakes has not been so far established, however. What distinguishes wakes from wall-bounded flows, and also from other free shear flows, is the presence of the vortex street, which for a small range of the Reynolds number (roughly 40 to 200) remains two-dimensional, and persists as the primary feature of the flow even in the turbulent regime. It has been well established in recent years that the vortex street is the nonlinear evolution of the absolute instability mode of the time-average flow in the wake (see among others, Koch 1985; Triantafyllou, Triantafyllou & Chryssostomidis 1986; Monkewitz & Nguyen 1987; Unal & Rockwell 1988; Hanneman & Oertel 1989; Karniadakis & Triantafyllou 1989; Strykowsky & Sreenivasan 1990). It is natural therefore to inquire first whether the absolute instability of the two-dimensional time-average flow can, above a certain Reynolds number, take the form of a three-dimensional instability mode, and so explain the onset of three-dimensionality.

A recent investigation has shown however (Triantafyllou 1990) that the absolute instability mode can become three-dimensional only if the *time-average* flow itself becomes three-dimensional. Thus, in two-dimensional geometries, three-dimensionality can only be caused by the appearance, above a certain Reynolds number,

of a secondary instability mechanism, which acts on the saturated state of the primary two-dimensional instability. The resulting three-dimensional pattern also creates (through the action of the Reynolds stresses) a spanwise modulation in the time-average flow. This scenario is supported by the numerical simulations of Karniadakis & Triantafyllou (1990), who have studied the evolution of three-dimensional noise in the wake of a two-dimensional cylinder at Reynolds numbers close to 200. The main finding of that work is that noise maintains its three-dimensionality above a Reynolds number of approximately 175. Below this Reynolds number, the wake always returned to its two-dimensional state. However, the three-dimensional state was found to be a harmonic one, contrary to what has been observed in other secondary instabilities. This shows that there is an important difference between the secondary instability of wakes and other (primarily wall-bounded) flows, in that it results in a soft loss of stability of the two-dimensional flow. Additional bifurcations have to take place before the wake reaches a turbulent state.

The purpose of this paper is to perform a numerical study of the transition process in the wake of bluff objects. An extension of the spectral element methodology in three dimensions is introduced, where we employ mixed Fourier/Legendre expansions in the spanwise direction. A similar approach was employed successfully in studying turbulent channel flow at modest Reynolds numbers in Karniadakis (1989*a*, *b*), and recently in simulating turbulent flow over riblet-mounted surfaces (Chu, Henderson & Karniadakis 1991). The paper is organized as follows. In §2, the formulation of the problem and the numerical procedure are described. In §3 the onset of three-dimensionality is analysed as a secondary instability phenomenon. In §§4 and 5, the successive bifurcations of the three-dimensional wake are analysed as a function of the Reynolds number and the transition to a chaotic state is discussed. The conclusions are summarized and discussed in §6.

2. Formulation

We consider Newtonian fluids governed by the Navier–Stokes equations of motion under the incompressibility condition:

$$\frac{\partial \boldsymbol{v}}{\Delta t} + \boldsymbol{N}(\boldsymbol{v}) = -\frac{\boldsymbol{\nabla} p}{\rho} + Re^{-1}\boldsymbol{\nabla}^2 \boldsymbol{v} \quad \text{in} \quad \Omega, \tag{1a}$$

$$\boldsymbol{\nabla}\cdot\boldsymbol{v} = 0 \quad \text{in} \quad \Omega, \tag{1b}$$

where $\boldsymbol{v}$ is the velocity field ($\boldsymbol{v}(\boldsymbol{x}, t) = (u, v, w)$), p is the static pressure, and the Reynolds number is defined as $Re = U_\infty(2R)/\nu$ where U_∞ is the free-stream velocity, R is the cylinder radius, ν is the kinematic viscosity, and ρ is the fluid density. Here $\boldsymbol{N}(\boldsymbol{v}^n) = \frac{1}{2}[\boldsymbol{v}^n\cdot\boldsymbol{\nabla}\boldsymbol{v}^n + \boldsymbol{\nabla}\cdot(\boldsymbol{v}^n\cdot\boldsymbol{v}^n)]$ represents the nonlinear contributions written in skew-symmetric form for aliasing control (Horiuti 1987). For future use we also define the Strouhal number $St = f(2R)/U_\infty$, where f is the frequency of the oscillation.

Numerical solution of the above system of equations will be obtained in the three-dimensional domain Ω defined by the cylinder geometry in figure 2*a*, *b*. The cylinder has a radius $R = 1$ in non-dimensional units. The spanwise z-direction is homogeneous and thus periodic boundary conditions can be assumed in that direction at a distance L_z. A uniform profile $U_\infty = 1$ is prescribed upstream at a distance $X_1 = 6$, while mixed Neumann/viscous-sponge boundary conditions (Tomboulides, Israeli & Karniadakis 1991) are prescribed at the outflow; these conditions eliminate spurious numerical

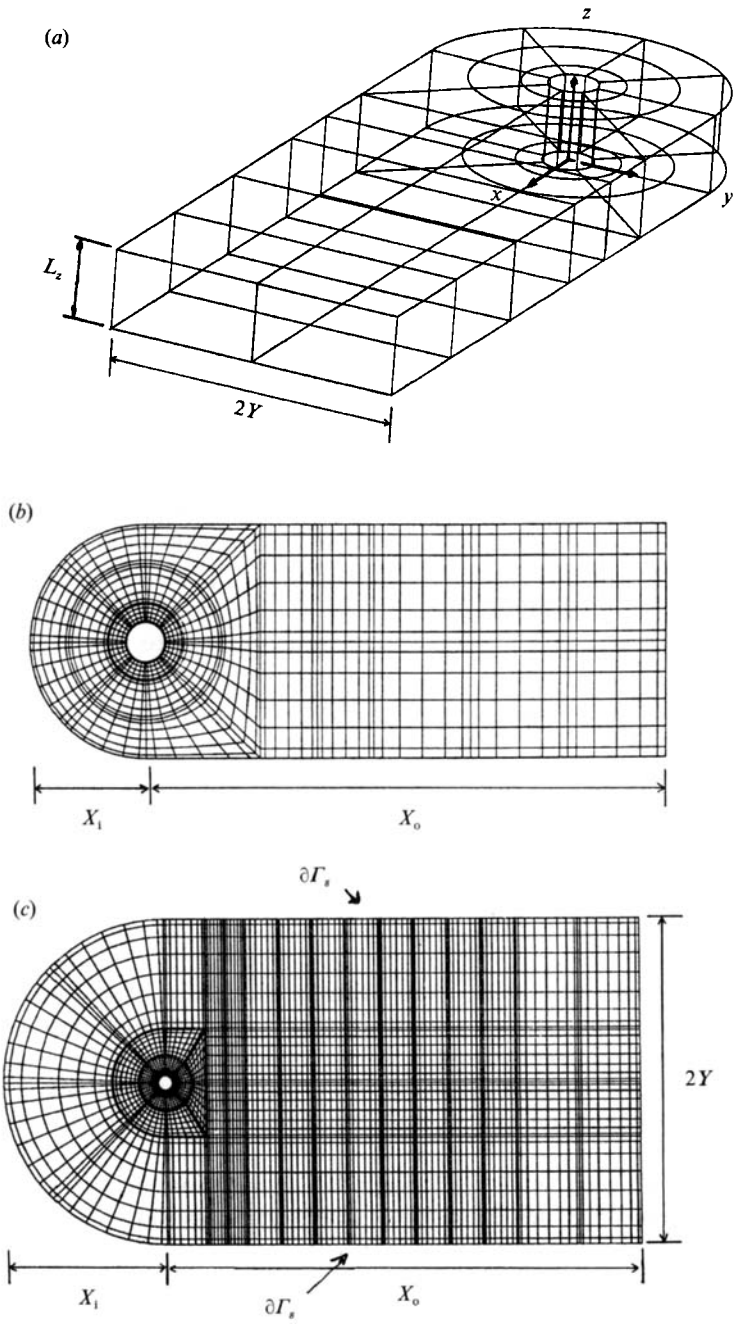

FIGURE 2. (*a*) A skeleton of the computational domain and geometry definitions. (*b*) A two-dimensional projection of the domain showing the spectral element discretization (domain D_0). (*c*) Spectral element mesh corresponding to the large domain D_1.

instabilities at the downstream boundary even at very high Reynolds number and provide better accuracy than the previously employed outflow boundary conditions (Karniadakis & Triantafyllou 1989).

Taking into account the homogeneity of the geometry in the spanwise z-direction

a significant simplification can be achieved if Fourier expansions are employed to represent data and field variables in that direction. A similar approach used in Karniadakis (1989*a*, *b*) and Chu *et al.* (1991) proved very efficient in direct simulations of turbulent flows in complex geometries. The dependent variables, for example, can then be represented as

$$\begin{Bmatrix} u(x,y,z,t) \\ v(x,y,z,t) \\ w(x,y,z,t) \\ p(x,y,z,t) \end{Bmatrix} = \sum_{m=0}^{M-1} \begin{Bmatrix} u_m(x,y,t) \\ v_m(x,y,t) \\ w_m(x,y,t) \\ p_m(x,y,t) \end{Bmatrix} e^{i\beta m z}, \tag{2}$$

where the spanwise wavenumber is defined as $\beta = 2\pi/L_z$, and is typically selected on the basis of two-point correlations. Here we choose $L_z = \pi, 2\pi$ which corresponds to $\beta = 2, 1$, respectively. This value of the spanwise length is close to the value used in direct simulations of turbulence in smooth channel flows. Unfortunately, there are no definite experimental results for spanwise correlations of cylinder wakes at low Reynolds number to justify our selection (see also §6).

Introducing now the Fourier expansions (2) into (1*a*) and taking the Fourier transform of (1*a*) (or equivalently following a Galerkin projection with test functions $\psi_z = e^{-i\beta m z}$) we arrive at the equivalent of (1*a*) discrete in z in the form

$$\frac{\partial \boldsymbol{v}_m}{\Delta t} + \boldsymbol{F}_m[\boldsymbol{N}(\boldsymbol{v})] = -\frac{\tilde{\boldsymbol{\nabla}} p_m}{\rho} + Re^{-1}[\nabla^2_{xy} - m^2\beta^2]\,\boldsymbol{v}_m \quad \text{in} \quad \Omega_m, \tag{3a}$$

$$\tilde{\boldsymbol{\nabla}} \cdot \boldsymbol{v}_m = 0 \quad \text{in} \quad \Omega_m. \tag{3b}$$

Here we have introduced the operators $\tilde{\nabla}$ and ∇^2_{xy} defined as

$$\tilde{\boldsymbol{\nabla}} = \left(\frac{\partial}{\partial x}, \frac{\partial}{\partial y}, im\beta\right), \qquad \nabla^2_{xy} = \frac{\partial^2}{\partial^2 x} + \frac{\partial^2}{\partial^2 y}, \tag{4a, b}$$

and $\boldsymbol{F}_m$ is the m-component of the Fourier transform of the nonlinear terms. The computational domain Ω_m is simply an (x,y)-plane of the domain Ω, and thus here all Ω_m are identical (see figure 2*b*). A similar approach has been developed recently for axisymmetric geometries, where Fourier expansions are employed in the azimuthial direction; details of this implementation can be found in Tomboulides (1992).

Before we proceed with the spatial discretization in the (x,y)-plane for each Fourier mode m of (3) we consider in the next subsection their time-discretization.

2.1. *Semi-discrete formulation*

The time-discretization of the governing equations (1) employs a high-order splitting algorithm based on mixed stiffly stable schemes (Karniadakis *et al.* 1991; Tomboulides, Israeli & Karniadakis (1989). Considering first the nonlinear terms we obtain for each Fourier component

$$\frac{\hat{v}_m - \sum_{q=0}^{J-1} \alpha_q \boldsymbol{v}_m^{n-q}}{\Delta t} = -\sum_{q=0}^{J-1} \beta_q \boldsymbol{F}_m[\boldsymbol{N}(\boldsymbol{v}^{n-q})] \tag{5a}$$

and α_q, β_q are implicit/explicit weight-coefficients for the stiffly stable scheme of

order J (see Karniadakis *et al.* 1991). The next substep incorporates the pressure equation and enforces the incompressibility constraint:

$$\frac{\hat{\tilde{v}}_m - \hat{v}_m}{\Delta t} = -\tilde{\nabla} p_m^{n+1}, \tag{5b}$$

$$\tilde{\nabla} \cdot \hat{\tilde{v}}_m = 0. \tag{5c}$$

Finally, the last substep includes the viscous corrections and the imposition of the boundary conditions, i.e.

$$\frac{\gamma_0 v_m^{n+1} - \hat{\tilde{v}}_m}{\Delta t} = Re^{-1} [\nabla_{xy}^2 - m^2\beta^2] v^{n+1}, \tag{5d}$$

$$v_0 = v_{\Gamma_0} \quad \text{and} \quad v_m = 0 \quad \forall m \neq 0, \tag{5e}$$

where γ_0 is a weight coefficient of the backwards differentiation scheme employed (Karniadakis *et al.* 1991), and v_{Γ_0} is the prescribed velocity on the boundary Γ_0.

The above time treatment of the system of equations (3) results in a very efficient calculation procedure as it decouples the pressure and velocity equations as in (5*b*, *c*) and (5*d*) respectively. In addition, it eliminates entirely the so-called time-splitting errors that result to non-zero divergence at Dirichlet boundaries (Tomboulides *et al.* 1989). As regards time accuracy of this splitting scheme, a key element in this approach is the specific treatment of the pressure equation (5*b*, *c*), which can be recast in the form

$$[\nabla_{xy}^2 - m^2\beta^2] p_m^{n+1} = \tilde{\nabla} \cdot \left(\frac{\hat{v}_m}{\Delta t} \right) \tag{6a}$$

along with the consistent high-order pressure boundary condition (see Karniadakis *et al.* 1991)

$$\frac{\partial p_m^{n+1}}{\partial n} = -\boldsymbol{n} \cdot \left[Re^{-1} \sum_{q=0}^{J-1} \beta_q (\tilde{\nabla} \times (\tilde{\nabla} \times v_m^{n-q}) + \sum_{q=0}^{J-1} \beta_q \boldsymbol{F}_m[\boldsymbol{N}(v^{n-q})] \right], \tag{6b}$$

where $\boldsymbol{n}$ denotes the unit normal to the boundary Γ_m. The resulting scheme provides accuracy of order J in time, in contrast to the classical splitting scheme where only first-order accuracy is achieved irrespective of the integration schemes involved at each substep.

Equation (6) is a Helmholtz equation for the pressure mode p_m^{n+1}; for $m = 0$ the pressure matrix is singular, indicative of the existence of one hydrostatic mode, while non-zero wavenumbers correspond to a non-singular pressure matrix (Karniadakis 1989*a*). Let $\phi = p_0^{n+1}$ and $g(\boldsymbol{x}) = \tilde{\nabla} \cdot (\hat{v}_0 / \Delta t)$, then (6) is a standard Poisson equation of the form

$$\nabla^2 \phi = g(\boldsymbol{x}) \tag{7}$$

along with a zero Neumann condition (for simplicity) replacing equation (6*b*). As this latter equation dictates the continuity requirements for the solution, we briefly review its spatial discretization in the next section.

2.2. *Spectral element methodology*

The spatial discretization of (5*a*), (5*d*), and (6) is obtained using the spectral element methodology (see, for example, Patera 1984, Karniadakis *et al.* 1985, Maday & Patera 1989 and Karniadakis 1989*a*, *b*; a review of recent advances of the method

is contained in Karniadakis *et al.* 1991*b*). Here we follow two different approaches. In the first, the formulation developed in the previous section is followed and thus two-dimensional spectral elements are considered in discretizing the (x,y)-planar domains Ω. Alternatively, a three-dimensional implementation of (5), (6) is also possible where the domain Ω is discretized using general hexaedra elements as in Karniadakis *et al.* (1985) and Maday & Patera (1989). This latter approach although less efficient for the current simulation is nevertheless more general as it also accommodates the case of non-periodic boundary conditions in the spanwise direction and has been used primarily in the current work. More specifically, in the standard spectral element discretization the computational domain Γ_m or Ω is broken up into several quadrilaterals in two dimensions or general brick elements in three dimensions, which are mapped isoparametrically to canonical squares or cubes respectively. Field unknowns and data are then expressed as tensorial products in terms of Legendre–Lagrangian interpolants. The final system of discrete equations in then obtained via a Galerkin variational statement.

To illustrate the spectral element methodology in more detail let us first consider the model equation, (7), which represents the elliptic contributions of the governing equations. Consideration of this model equation rather than the hyperbolic equation (5*a*) corresponding to the convective terms suggests a 'layered' approach, according to which the discretizations and solvers are constructed on the basis of a hierarchy of nested operators proceeding from the highest to the lowest derivatives. This approach is motivated by the fact that the highest derivatives in an equation govern the continuity requirements, conditioning, and stability of the system.

For simplicity we only present the two-dimensional spectral element equations, as the Galerkin spectral formulation in the spanwise direction can be found in Gottlieb & Orszag (1977). In addition, we assume homogeneous boundary conditions $\phi = 0$ on Γ. Equation (7) can then be discretized using planar spectral elements in the (x,y)-plane. If we define H_0^1 as the standard Sobolev space that contains functions which satisfy homogeneous boundary conditions, and introduce test functions $\psi \in H_0^1$, we can write the equivalent variational statement of (7) as

$$\int_\Omega \nabla\phi \cdot \nabla\psi \, \mathrm{d}s = -\int_\Omega \psi g \, \mathrm{d}s. \tag{8}$$

The spectral element discretization corresponds to numerical quadrature of the variational form (8) restricted to the space $X_h \subset H_0^1$. The discrete space X_h is defined in terms of the spectral element discretization parameters (K, N_1, N_2), where K is the number of 'spectral elements', and N_1, N_2 are the degrees of piecewise high-order polynomials in the two directions respectively that fill the space X_h. By selecting appropriate Gauss–Lobatto points ξ_{pq}^k and corresponding weights $\rho_{pq} = \rho_p \rho_q$, equation (8) can be replaced by

$$\sum_{k=1}^{K} \sum_{p=0}^{N_1} \sum_{q=0}^{N_1} \rho_{pq} J_{pq}^k \nabla\phi \nabla\psi]_{\xi_{pq}^k} = -\sum_{k=1}^{K} \sum_{p=0}^{N_1} \sum_{q=0}^{N_1} \rho_{pq} J_{pq}^k [\psi g]_{\xi_{pq}^k}. \tag{9}$$

Here J_{pq}^k is the Jacobian of the transformation from global to local coordinates $(x,y) \Rightarrow (r,s)$, for the two-dimensional element k. The Jacobian is easily calculated from the partial derivatives of the geometry transformation r_x, r_y, s_x, s_y. The next step in implementing (9) is the selection of a basis which reflects the structure of the piecewise smooth space X_h. We choose an interpolant basis with components defined in terms of Legendre–Lagrangian interpolants, $h_i(r_j) = \delta_{ij}$. Here, r_j represents a local

coordinate and δ_{ij} is the Kronecker-delta symbol. It was shown in Patera (1984) and Rønquist (1988) that such a spectral element implementation converges spectrally fast to the exact solution for a fixed number of elements K and $N_{1,2,3} \to \infty$, for smooth data and solution, even in non-rectilinear geometries.

Having selected the basis, we can proceed in writing the local to the kth element spectral approximations for ϕ^k, (or ψ^k) as follows:

$$\phi^k = \phi^k_{mn}\, h_m(r)\, h_n(s) \quad \forall m, \quad n \in (0, \ldots, N_1), (0, \ldots, N_2), \tag{10a}$$

where ϕ^k_{mn} is the local nodal value of ϕ. The geometry is also represented via similar type tensorial products with same-order polynomial degree, i.e.

$$(x, y)^k = (x^k_{mn}, y^k_{mn})\, h_m(r)\, h_n(s) \quad \forall m, \quad n \in (0, \ldots, N_1), (0, \ldots, N_2). \tag{10b}$$

Here x^k_{mn}, y^k_{mn} are the global physical coordinates of the node mn in the k element. This isoparametric mapping leads to a compatible pressure formulation without the presence of spurious modes due to the ellipticity property of the pressure equation (Karniadakis 1989*a*).

We now insert (10) into (9) and choose test functions ψ_{mn} which are non-vanishing at only one global node to arrive at the discrete matrix system. This procedure is straightforward and here we cite only the final matrix system,

$$\sum_{k=1}^{K}{}' \sum_{m=0}^{N_1} \sum_{n=0}^{N_2} (P^{x,k}_{ijmn} + P^{y,k}_{ijmn})\, \phi^k_{mn} = -\sum_{k=1}^{K}{}' \sum_{m=0}^{N_1} \sum_{n=0}^{N_2} J^k_{ij} B^k_{im} B^k_{jn} g^k_{mn}, \tag{11a}$$

where the prime denotes direct stiffness summation for the global system to ensure that the ensemble is performed in space H^1. The x-component, for example, of the Poisson operator is defined as follows:

$$\begin{aligned} P^{x,k}_{mn} = \rho_{pq} J^k_{pq} [& (r_x)^2_{pq}\, \mathrm{D}_{pi}\, \mathrm{D}_{pm}\, \delta_{nq} + (s_x)^2_{pq}\, \mathrm{D}_{qj}\, \mathrm{D}_{qn}\, \delta_{mp} \\ & + (r_x s_x)_{pq}\, \mathrm{D}_{pi}\, \mathrm{D}_{qn}\, \delta_{mp} + (r_x s_x)_{pq}\, \mathrm{D}_{qj}\, \mathrm{D}_{pm}\, \delta_{nq}]. \end{aligned} \tag{11b}$$

Here the derivative operator is defined as $\mathrm{D}_{ij} = (\mathrm{d}h_j/\mathrm{d}z)\,(\xi_i)$; all other parameters have been defined previously. The mass matrix B^k_{ij} is diagonal and is defined as $B^k_{ij} = \rho_i \delta_{ij}$. The y-component of the Poisson operator is defined similarly.

The natural choice of solution algorithm for (11*a*) is an iterative procedure; both conjugate gradient techniques and multigrid methods have been implemented for elliptic equations (Rønquist 1988). For the spectral element–Fourier algorithm the use of a parallel static condensation solver enhances the efficiency even further (see (Chu *et al.* 1991). The advantage of the formulation proposed here compared to the formulation proposed by Rønquist is that the high-order splitting scheme results in separate, elliptic equations for the pressure and velocity that can be very efficiently and robustly solved using those iterative techniques without the need of case-dependent preconditioners or other convergence acceleration techniques.

2.3. *Simulation tests*

Before we proceed with the numerical investigation of the three-dimensional flow, we first report on some tests we performed to assess the influence of the computational domain. To this purpose we used the domain of figure 2(*b*) to compute the two-dimensional flow at Reynolds number of 100, for which we have extensive results obtained using domains of different size both in the x- and y-directions, as well as different numbers of elements and orders of interpolation. An additional objective is

Domain	BC on $\partial\Gamma_s$	X_0	X_i	Y	St
D_0	periodicity	27	−6	6	0.204
D_1	periodicity	70	−24	24	0.168
D_2	periodicity	36	−24	24	0.168
D_3	potential	27	−6	6	0.188
D_4	potential	57	−6	6	0.188
D_5	potential	27	−12	12	0.174
D_6	potential	27	−12	7	0.182
D_7	periodicity	50	−10	10	0.179

TABLE 1. The periodic boundary condition compared to Dirichlet boundary conditions corresponding to the potential flow solution

to investigate the discrepancy in Strouhal number between our earlier computations (Karniadakis & Triantafyllou 1989) and the experimentally measured values (Williamson 1989; Hammache & Gharib 1989).

The size of a two-dimensional computational domain around a cylinder is described by three characteristic dimensions: (i) the outflow length X_0 which specifies where the downstream boundary is located; (ii) the inflow length X_i which specifies where the inflow boundary is located; and (iii) the half-width of the domain (size in the y-direction) denoted by Y. The periodicity boundary condition imposed along the side was also tested and compared to Dirichlet boundary conditions corresponding to the potential flow solution. The results are summarized in table 1, while a typical spectral element mesh more refined than the one shown in figure 2(*b*) is shown in figure 2(*c*). For this mesh and domain D_1 ($X_0 = 70$; $X_i = Y = 24$) the corresponding Strouhal frequency is $St = 0.168$; this value remains unaffected if the shorter domain D_2 is employed in the simulation. The experimental value at this Reynolds number is obtained using the empirical formula of Williamson (1989, equation (6)) is $St = 0.165$, and thus there is a discrepancy of approximately 1.5%; our earlier simulations corresponding to domain D_7 (Karniadakis & Triantafyllou 1989) gave $St = 0.179$.

A simulation was next performed using the domain of figure 2(*b*), with the potential flow solution imposed as boundary condition at the sides (domain D_3). The difference in frequency with the one obtained from domain D_0 (that used in the three-dimensional simulations) is about 7%. This frequency remains unaffected even if a much longer domain D_4 with $X_0 = 57$ is used, consistent with our previous results for the wider domains (D_1, D_2). Further experimentation with variations in the inflow length and the width of the domain (D_4–D_7) indicate that decreasing the inflow length increases the value of the Strouhal number. Finally, a simulation was performed using the same domain, but with higher resolution per element (9×9) and smaller time step Δt, and gave identical results. This last test confirms that the discrepancy between experiment and computation is caused, barring measuring errors in experiments, by the size and shape of the computational domain, not by inaccuracies of the spectral element scheme.

From table 1, it can be verified that the domain chosen for numerical expediency introduces an error in the vortex-shedding frequency of around 15%. Shifts in the values of critical Reynolds numbers (i.e. Reynolds numbers marking flow bifurcations) caused by the size of the domain are more difficult to assess. Judging from the critical Reynolds number for the onset of three-dimensionality, it would appear that the shift also lies within the same margins of error: our numerical

estimate of that value is between 200–210 (see §3), whereas the experimental value (Williamson 1988) is around 180.

Having discussed the numerical methodology employed in the current investigation, we now analyse the results of the three-dimensional simulation. Both full three-dimensional and spectral element–Fourier discretizations were used; the latter is more efficient than the former, resulting in savings in CPU time of more than one order of magnitude. Sixth- and eighth-order interpolants ($N_{1,2} = 7, 9$) were used in the spectral elements, and $N_3 = M = 16$ modes in the spanwise direction (some tests were also performed with $M = 32$ modes; Tomboulides 1992); the number of elements was kept constant for the three-dimensional simulation ($K = 34$). The corresponding CPU requirement is approximately two seconds per time step on a single processor CRAY-Y/MP.

3. Onset of three-dimensionality

3.1. *Numerical experiments*

The onset of three-dimensionality was investigated first, by expanding the findings of our previous three-dimensional simulation (Karniadakis & Triantafyllou 1990). The flow past a cylinder at $Re = 225$ was thus computed, and three-dimensional noise was subsequently introduced. The noise was introduced by temporarily increasing the tolerances in the pressure and velocity residual, equations (5). After some initial transient the tolerances were reduced to machine accuracy. The subsequent evolution of the flow was followed through direct simulation of the three-dimensional Navier–Stokes equations. The spanwise, i.e. parallel to the cylinder axis, component of the instantaneous velocity was used as a measure of the three-dimensionality of the flow. (In a two-dimensional flow this component is equal to zero.) More precise measures of three-dimensionality can also be used to determine the exact location where it sets in (see Kaiktsis *et al.* 1991); however, we have found that monitoring the evolution of the spanwise velocity component as a function of time leads to the same conclusions.

The rationale behind the excitation procedure is as follows. At below the critical Reynolds number, the two-dimensional vortex street is the only attracting limit cycle, and the perturbed flow always returns to it. Above the critical Reynolds number, other attracting limit cycles exist, oscillating around spanwise modulated average flows. The perturbed flow will thus be attracted to these three-dimensional states, in the process causing a spanwise simulation of the time-average flow.

At $Re = 175$, the noise dies out, and the flow asymptotically returns to its two-dimensional state, indicating that no secondary instability is present (see figure 3*a*, *b*). At $Re = 225$, however, the noise is amplified in time and evolves into a coherent three-dimensional pattern (figure 4, plate 1); the presence of a secondary instability can thus be inferred. The time-evolution of the spanwise velocity component shows the action of the secondary instability best: out of an initially random noise, one specific pattern is selected through exponential amplification in time (figure 5*b*). The growth of the instability is saturated by nonlinearities, and the flow settles into a periodic limit cycle. The time trace of the w-component close to the centreline in the wake (figure 6*a*) shows the presence of the fundamental frequency and its higher harmonics. The other two components show mainly the presence of the Strouhal frequency, as can be seen for example in the time trace of the streamwise component (figure 5*a*, 6*b*). The secondary instability results therefore at this Reynolds number to a switching from a two-dimensional to a three-dimensional mode of self-

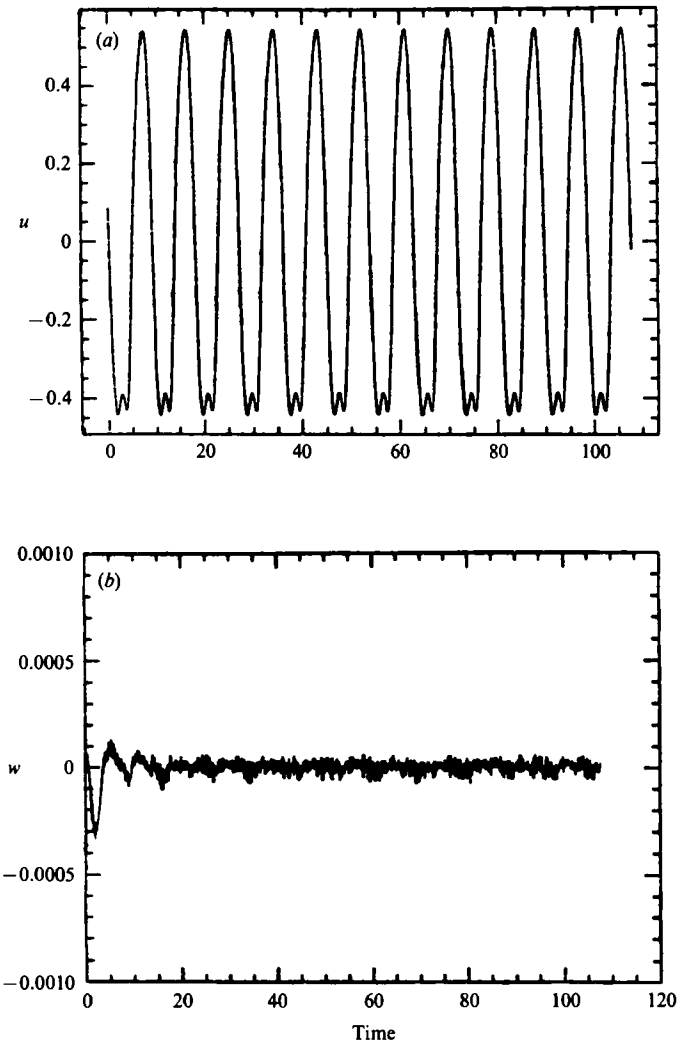

FIGURE 3. Time history of the velocity components at $x = 2.0$; $y = 0.15$; $z = 0$ and $Re = 175$; $\beta = 2.0$. (*a*) Streamwise and (*b*) spanwise components.

oscillation. In laboratory experiments, where the velocity is slowly increased as a function of time, hysteresis phenomena are possible for Reynolds numbers around 200 (Williamson 1988). For a sufficient slow increase in the velocity, which also implies slow variation of the Reynolds number, the secondary instability may be delayed. Then the flow will remain two-dimensional even above $Re = 175$, but as the velocity is further increased, the flow suddenly 'jumps' into its three-dimensional mode. (Similar hysteresis phenomena can occur if the Reynolds number is lowered.) We have not, however, observed such hysteresis phenomena in the current simulations.

Finally, this simulation was repeated with the wider domain corresponding to spanwise wavenumber $\beta = 1$. The main finding is that the three-dimensional limit cycle remains essentially unaffected by the spanwise size in this range of Reynolds numbers. In particular, we found a limit cycle at $Re = 210$, 220 and 225. However, at $Re = 200$ the spanwise oscillations decayed to zero; it is thus concluded that, for

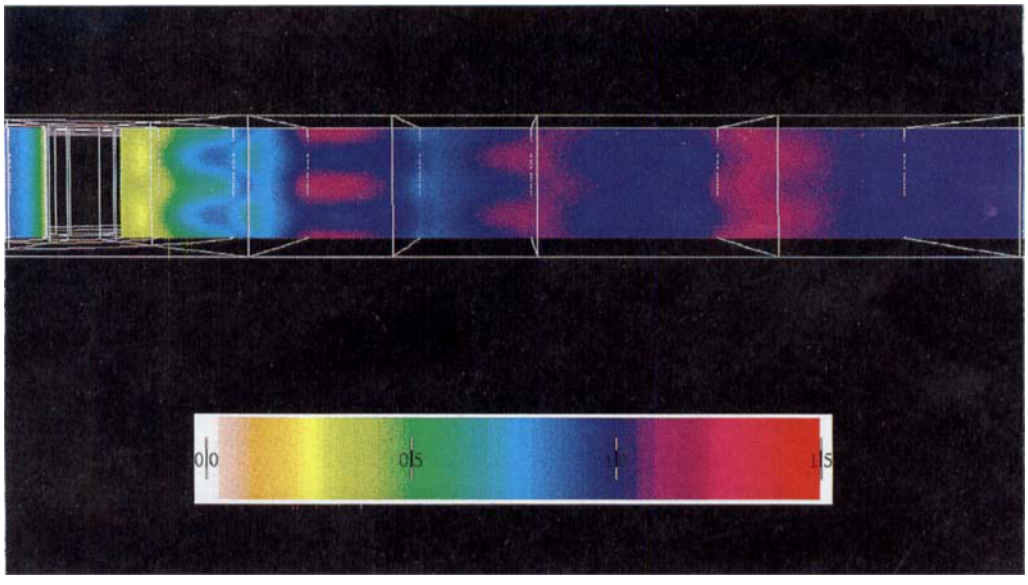

FIGURE 4. Instantaneous colour contours of the streamwise velocity field on the (x, z) centreline plane (Re=225).

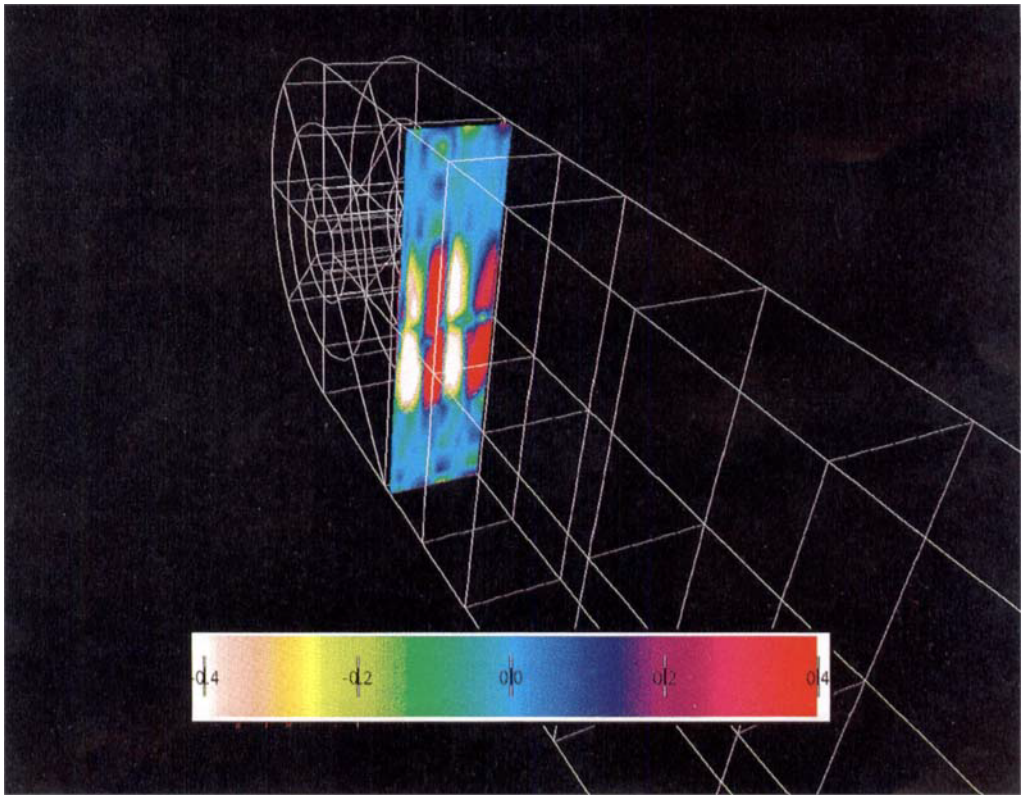

FIGURE 13. Instantaneous colour contours of the streamwise vorticity on a $(y, z)-$ plane at x=7 (Re=300).

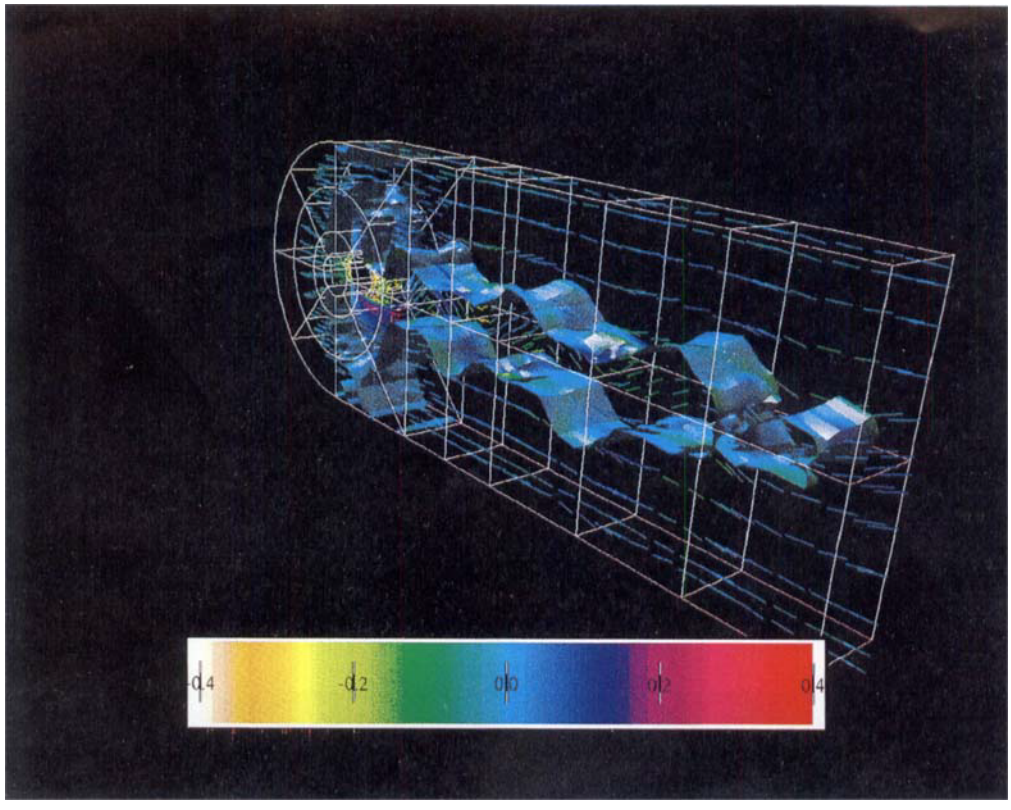

FIGURE 18. Instantaneous pressure iso-surface coloured according to the spanwise velocity magnitude (Re=500).

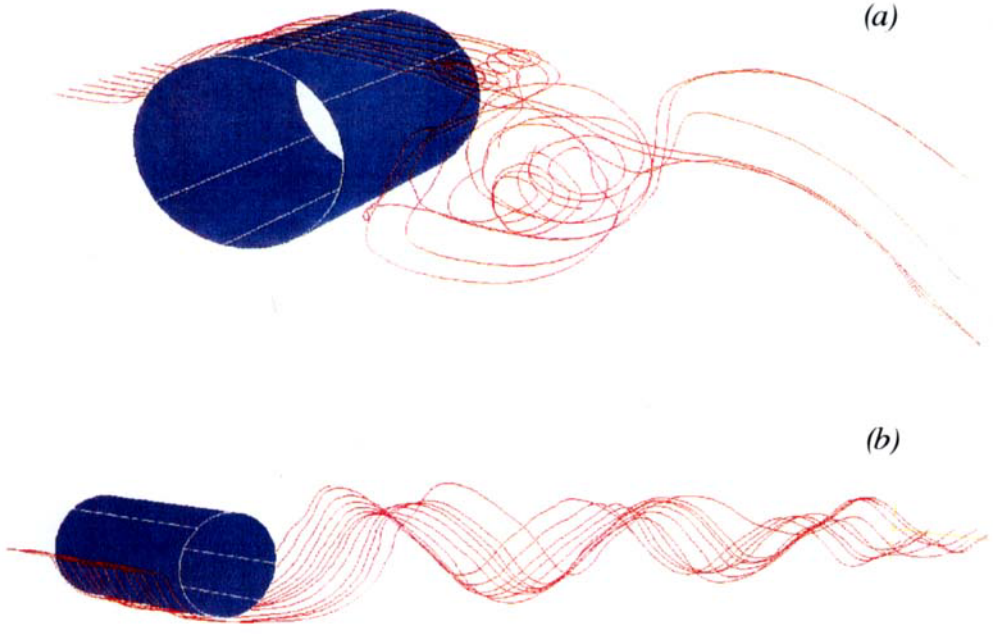

FIGURE 22. Instantaneous streamlines of the three-dimensional vortex street at Re=500, *(a)* in the near-wake and *(b)* far downstream.

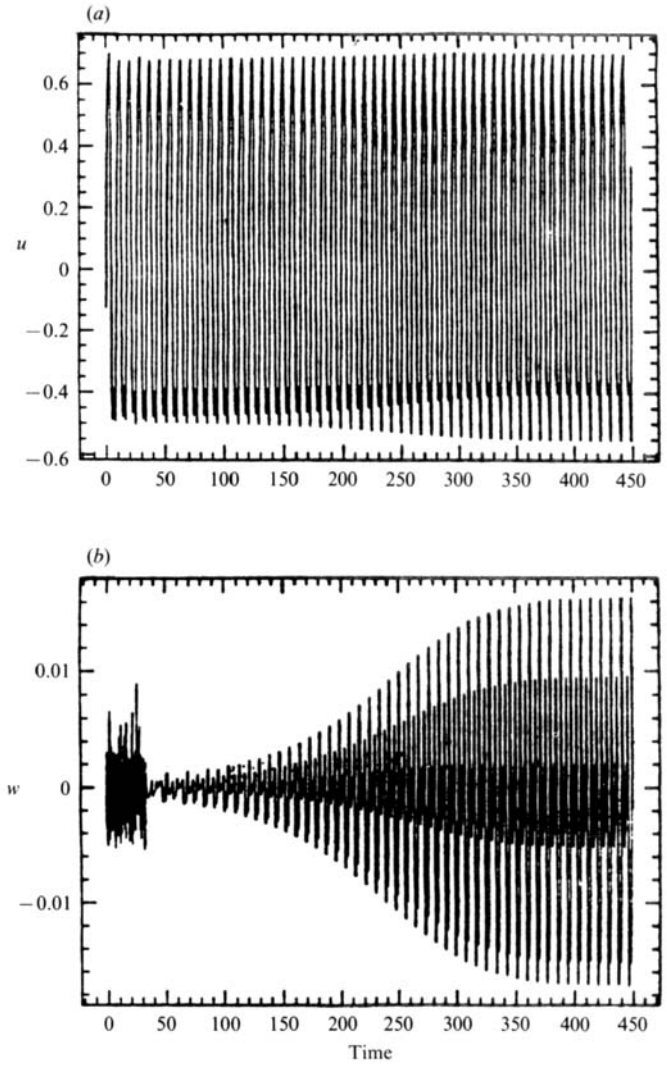

FIGURE 5. Time history of the velocity components at $x = 2.0$; $y = 0.15$; $z = 0$ and $Re = 225$; $\beta = 2.0$. (*a*) Streamwise and (*b*) spanwise components.

the computational domain used in this study, three-dimensionality first appears at a Reynolds number between 200 and 210. The exact value of the critical Reynolds number, Re_c^{3D}, above which three-dimensionality sets in is computationally very expensive to obtain using direct numerical simulation. The construction of low-dimensional models, however, from the direct simulation data in conjunction with the use of modern numerical bifurcation techniques could potentially be an effective approach in computing Re_c^{3D} (work in progress); this approach was followed recently by Deane *et al.* (1991) in studies of two-dimensional bifurcations in wake flows.

3.2. *Instability analysis*

The final three-dimensional flow pattern can be described as the *absolute instability* mode of its *time-average flow*. Assuming nearly parallel flow, the instability modes have the form of travelling waves in the streamwise direction, with an eigenfunction

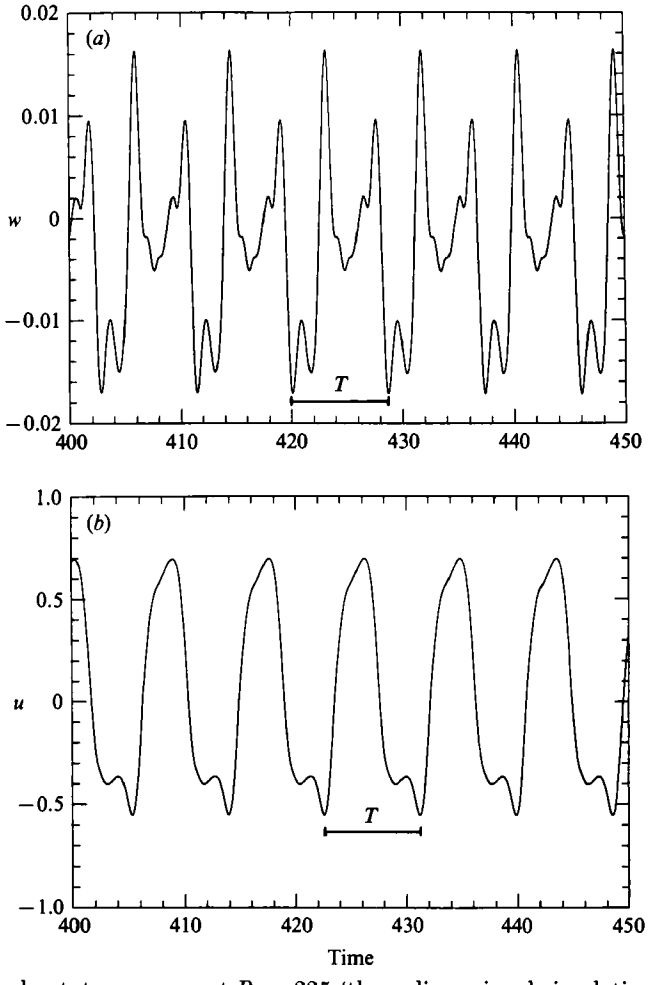

FIGURE 6. Steady-state response at $Re = 225$ (three-dimensional simulation) at point P_1. Time history of (*a*) w-component; (*b*) u-component.

dependence in the other two directions. By substituting perturbations of this form into the equations of motion and continuity, linearized around the modulated time-average flow, the dispersion relation is obtained. The resulting equations are

$$\mathrm{i}(kU-\omega)\,u' + v'\frac{\partial U}{\partial y} + w'\frac{\partial U}{\partial z} = -\mathrm{i}kp' + Re^{-1}[\nabla^2_{yz} - k^2]\,u', \tag{12a}$$

$$\mathrm{i}(kU-\omega)\,v' = -\frac{\partial p'}{\partial y} + Re^{-1}[\nabla^2_{yz} - k^2]\,v', \tag{12b}$$

$$\mathrm{i}(kU-\omega)\,w' = -\frac{\partial p'}{\partial z} + Re^{-1}[\nabla^2_{yz} - k^2]\,w', \tag{12c}$$

along with the continuity equation

$$\mathrm{i}ku' + \frac{\partial v'}{\partial y} + \frac{\partial w'}{\partial z} = 0. \tag{12d}$$

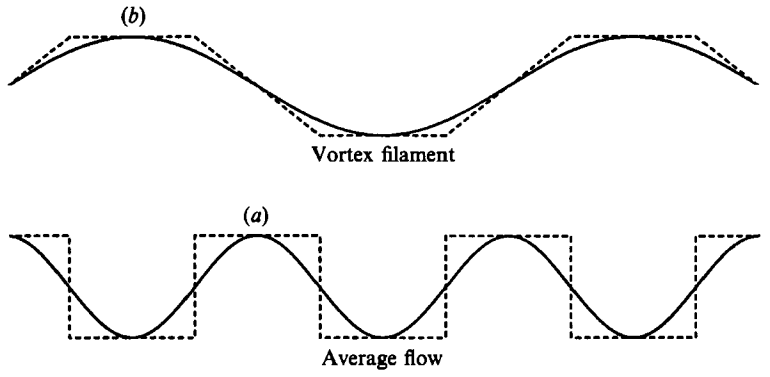

FIGURE 7. Qualitative description of the spanwise flow structure in the near wake at slightly supercritical states using vortex filaments. Curve (*a*) corresponds to time-average flow; curve (*b*) corresponds to the perturbation field.

Here, we denote the perturbation field by the vector (u', v', w'), and the Laplacian operator ∇^2_{yz} is defined as in (4*b*). The time-average velocity is denoted by $U(y,z)$, k is the streamwise wavenumber, and ω is the frequency of the instability wave.

Equations (12), subject to the periodicity condition in the z-direction, and the constraint that the perturbation vanishes at the boundaries of the flow in the y-direction, define an eigenvalue problem for the frequency ω, once the wavenumber k is specified. The problem can be solved numerically to determine the frequency ω as a function of the wavenumber k. Then, the 'pinch-points' (Bers 1983) of the dispersion relation can be obtained by mapping the complex k-plane into the complex ω-plane, as discussed in Triantafyllou *et al.* (1986). Classification of the pinch points will identify the character of instability that produces the three-dimensional pattern. This procedure is however very cumbersome for the problem at hand, since it requires the solution of several high-order eigenvalue problems. A much simpler approximation can be derived, assuming a weak modulation of the time-average flow in the spanwise direction, which has the advantage of better elucidating the physics of the problem. This can be done by approximating the actual mode by a slowly varying mode in the spanwise direction, using the following procedure (Triantafyllou 1990). At Reynolds numbers very close to the onset of the secondary instability the time-average flow has the following form:

$$U(y,z) = U_0(y) + u_1(y)\cos(\beta z), \tag{13}$$

where u_1 is much smaller than U_0 in magnitude. Consequently, the derivatives of U with respect to z are one order of magnitude smaller than the derivatives of U with respect to y. We can, to a first approximation, neglect the derivatives of U with respect to z; this assumption is valid at a state slightly above criticality. In this case, the equations above can be combined into the classical Orr–Sommerfeld equation for three-dimensional perturbations (Drazin & Reid 1981), with the important difference that the base velocity U is a slowly varying function of the coordinate z.

We can therefore talk of 'less' unstable flow regions, where the flow reversal in the wake is smaller, and 'more' unstable flow regions, where the flow reversal is stronger. These regions can be identified by solving the Orr–Sommerfeld equation for a given wavenumber at various locations, and then plotting the growth rate of the Orr–Sommerfeld equation as a function of z. The resulting growth rate will follow the modulation of the time-average flow, as schematically shown in curve (*a*) in figure 7. Because of Squire's transformation (Squire 1933), the only way that a single-

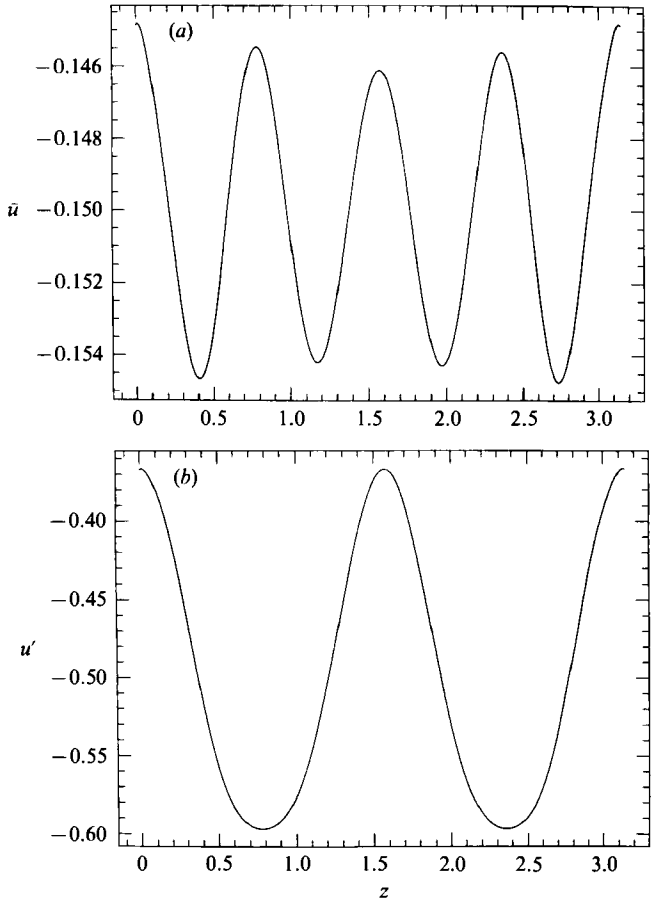

FIGURE 8. Spanwise variation of the streamwise velocity component in the near wake ($x = 2.0$; $y = 0$) and $Re = 225$. (*a*) Time-average field $\bar{u}$, (*b*) perturbation field $u' = u - \bar{u}$. Here $u(x, y, z, t)$ is the instantaneous streamwise velocity component.

	z-Location	Frequency	Growth rate
1	1.0	0.242	0.1703
2	1.5	0.237	0.1661
3	2.0	0.247	0.1731
4	2.5	0.240	0.1693

TABLE 2. 'Pinch-point' of dispersion relation at different z-locations ($x = 2.0$) corresponding to the time-average three-dimensional flow at $Re = 225$

frequency three-dimensional pattern can satisfy the slowly varying Orr–Sommerfeld equation throughout the span is by being two-dimensional in the least unstable flow regions, in order to achieve the maximum local growth rate, and by being sufficiently three-dimensional in the more unstable flow region so that it can have the same growth rate and frequency as in the less unstable region. In fact, the maximum transverse wavenumber will appear at the most unstable flow location. The spanwise variation of the instability mode is schematically plotted as curve (*b*) in figure 7, where the aforementioned relation between the maxima and minima of the growth

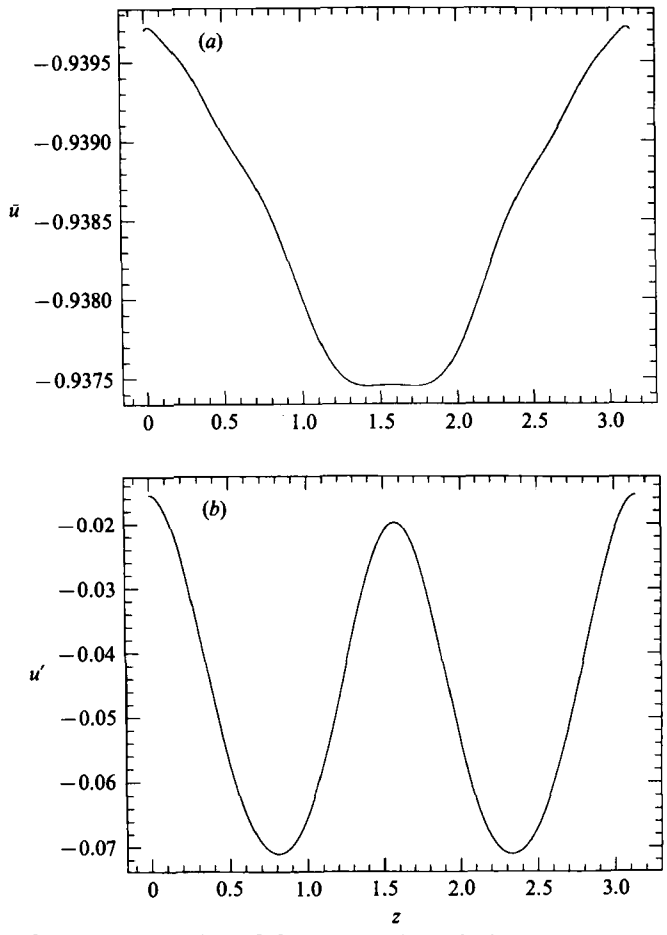

FIGURE 9. Spanwise variation of the streamwise velocity component at $x = 10$; $y = 0$ and $Re = 225$. (*a*) Time-average field $\bar{u}$, (*b*) perturbation field $u' = u - \bar{u}$.

rate and the inclination of the instability mode can be seen. Figure 7 also shows that the spanwise wavelength of the perturbation flow is equal to twice that of the time-average flow.

We thus have the interesting conclusion that the dispersion relation of the modulated time-average flow can, to leading order in the modulation, be approximated by the dispersion relation of a fictitious two-dimensional flow at the location $z = z_m$ where the growth rate has a minimum. This also implies that the Strouhal frequency is determined by the pinch-point double-root of this approximate dispersion relation. Since the flow at $z = z_m$ is less unstable than the two-dimensional one at the same Reynolds number, this implies that the Strouhal frequency of the three-dimensional mode is lower than that of the two-dimensional flow at the same Reynolds number, consistently with experimental findings (Williamson 1988). In other words, switching from the two- and three-dimensional mode of self-oscillation in the wake results in a sudden reduction in the Strouhal number.

In order to verify this approximate in stability theory, we have looked at the instability properties of the wake as a function of the spanwise coordinate z. Thus with the streamwise distance x kept constant, and equal to one cylinder diameter, the time-average velocity was computed as a function of the coordinate y for four

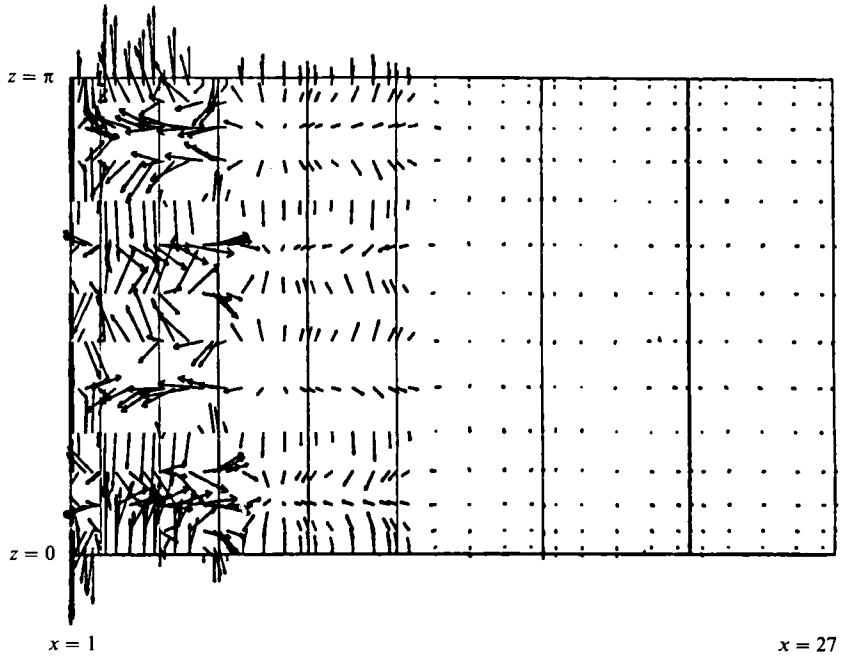

FIGURE 10. Two-dimensional projection on the (x, z)-plane at $y = 0$ of the vorticity vector field ($Re = 225$).

values of z along the spanwise direction at $Re = 225$. At each location the pinch point of the dispersion relation was then computed, the latter consisting of the Orr–Sommerfeld equation with boundary conditions at the ends of the domain in the y-direction. The results are summarized in table 2. It can be seen that location 2, which is the least unstable of all four considered, gives $St = 0.237$, which is indeed the closest to the value of 0.234 found from the numerical simulation.

3.3. *Spatial evolution of the time-average flow*

The spanwise variations of the time-average and the perturbation flows in the near wake are compared next (figures 8*a* and 8*b*, respectively). The basic wavelength of the time-average flow is equal to half of that of the perturbation flow. Furthermore, the instantaneous flow is straight behind the regions corresponding to extrema of the time-average flow, in agreement with the linear instability arguments given above. The slight discrepancy in the peak values of velocity amplitude across the span is due to both time-averaging and spatial errors (Legendre expansions used along the spanwise direction in this computation). The use of Fourier expansions along the spanwise direction alleviates this discrepancy significantly (Tomboulides 1992).

The next question to consider is how far downstream this relation persists, since wavy vortex filaments tend to substantially change their form as they progress downstream (see also Meiburg & Lasheras 1988). The metamorphosis of the instantaneous flow will also alter the time-average flow through the action of the Reynolds stresses. The downstream evolution of the time-average flow in the present simulation showed a gradual change in the spanwise structure. At approximately five diameters downstream, the time-average flow (figure 9*a*) has very different structure, while the perturbation flow retains its near-wake form (figure 9*b*; see also figure 4).

As far as the space–time development of the flow is concerned a very important issue is the effect of the mechanisms of stretching and tilting of the vortex filaments, which in two-dimensional wakes are simply straight lines. Such issues are related to the development of spatial chaos, and the question is whether they play such a role in the wake. To assess the importance of these mechanisms, plan views of the vortex filaments, i.e. their projections on an (x, z)-plane, were computed. In figure 10 the projected vorticity field is visualized from the rear edge of the cylinder ($x = 1$) to the outflow. It is seen that the vorticity vectors are indeed wavy in the z-direction in the near wake, while further downstream they form rib-like structures, similar to the ones observed in compressible planar wakes (Chen *et al.* 1989) and shear layers (Metcalfe *et al.* 1987) (see also §4). These changes in form are tied to changes in the form of the time-average flow. The stretching and tilting mechanisms do not seem to affect the temporal periodicity of the flow, since the state of the flow remains periodic in the far field. This is indicated more clearly in figure 4 where we plot the spatial structure of the instantaneous u-velocity field.

4. The first period doubling

The flow at $Re = 300$ was next computed starting from the three-dimensional field obtained at $Re = 225$. The integration continued for a long time until transients between the two flow states were eliminated. At the new Reynolds number the flow has undergone a bifurcation that leads to a periodic state with a period of oscillation twice the fundamental one, present at $Re = 225$. This is exhibited best by the time trace of the w-component (figure 11*a*), which has a strongly modulated form, and to a lesser extent by the time traces of the other two components, which exhibit a weaker modulation (see for example the u-component in figure 11b). The power spectra of these two signals, shown in figures 11(*c*), 11(*d*) respectively (the spectrum of the v-component is very similar to that of u), reveal the presence of several frequencies, and most notably, that of a subharmonic. The spectrum of the w-component contains a very strong subharmonic peak, whereas the u, v velocity spectra contain a rather weak peak at the subharmonic. The phase-space plot of the three velocity components plotted against each other (figure 12*a*, *b*) shows the branching of the limit cycle that was present at $Re = 225$ into two stable limit cycles. The latter appear in the (u, v, w)-space as nearly planar curves lying on different planes.

The occurrence of a period doubling can be explained as follows. From the sketch in figure 7 it is clear that, once the secondary instability is triggered, there are two possible three-dimensional modes, which are equally acceptable. The first has the spanwise modulation shown in figure 7, and the second has the modulation of the first shifted by half a wavelength. It can readily be seen that this shifting preserves the relation (see the discussion in §3) between the maxima and minima of the local growth rate and the inclination of the vortex filaments. The period doubling is therefore caused by the fact that the flow alternates between these two states, and its period doubles. In the physical space, a vortex filament like the one in figure 7 is produced, then one (Strouhal) period later the alternative filament is produced, i.e. the filament of figure 7 shifted by half the spanwise wavelength, and one (Strouhal) period later the filament of figure 7 is produced again. The time required for a full cycle has thus doubled. In the phase space (figure 12), the two alternative states are the two out-of-plane curves, symmetric around the $w = 0$ plane.

It is worth mentioning that the period-doubling bifurcation does not lead to vortex

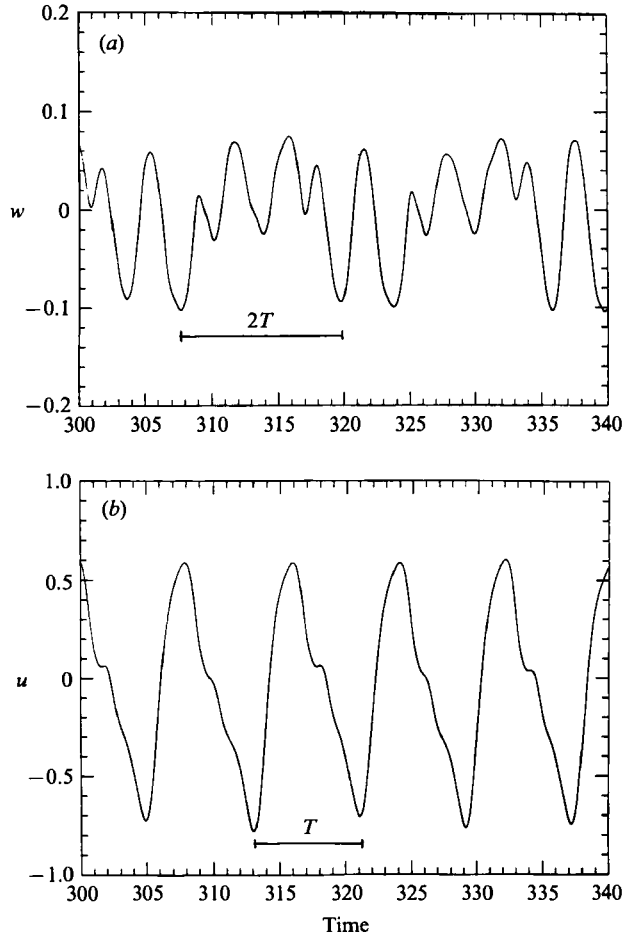

FIGURE 11 (a, b). For caption see facing page.

merging, and the wake retains its basic spatial structure. In contrast, in the apparently similar flow of a two-dimensional jet, the appearance of a subharmonic does imply vortex merging, as found by Batcho, Karniadakis & Orszag (1990). We attribute the difference to the fact that vortex merging is basically a two-dimensional subharmonic instability phenomenon, which is present in jet and shear layer flows but not in wakes. The spanwise flow structure can be best visualized instantaneously using contours of streamwise vorticity ω_x: in figure 13 (plate 1) colour contours of ω_x are plotted at approximately three cylinder diameters downstream of the cylinder centre. The rib-like structure shown in figure 10 at $Re = 225$ is more clear at this Reynolds number ($Re = 300$).

Finally, in order to investigate the effect of the width of the domain on the period-doubling bifurcation, the computation was repeated using a domain twice as wide ($L_z = 2\pi$). The presence of the subharmonic in the spectra of the velocity fluctuations can be detected again (figure 14). The important difference of the computation using the wider domain is that three-dimensionality has been increased, in the sense that the amplitude of the w-component has been increased.

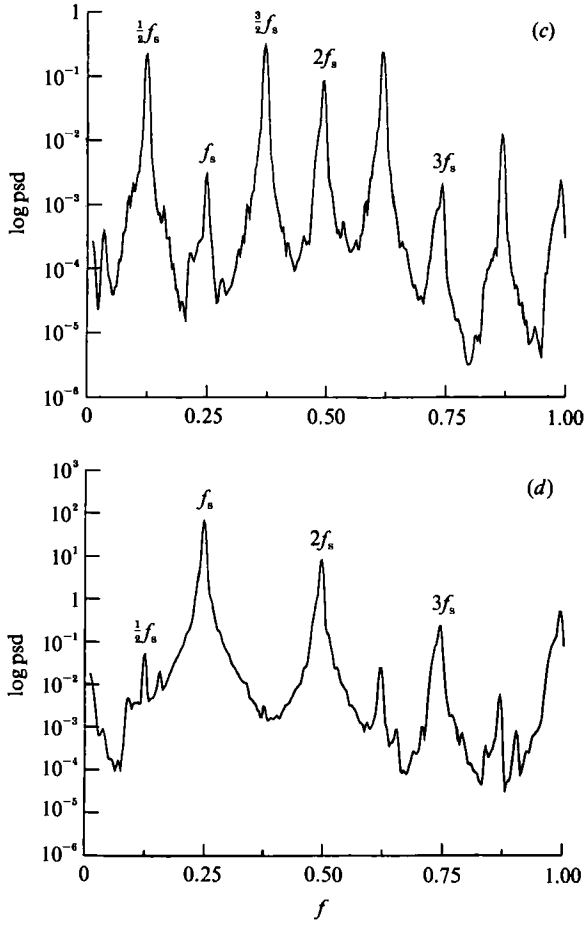

FIGURE 11. (*a*) Time-history of w-velocity at P_1 and $Re = 300$. (*b*) Time-history of u-velocity at P_1 and $Re = 300$. (Only a portion of the total time-traces are shown here.) (*c*) Power spectrum of trace plotted in (*a*). (*d*) Power spectrum of trace plotted in (*b*).

5. Transition to turbulence

The Reynolds number was next increased to 333, and the three-dimensional flow computed as previously described starting from the velocity field at $Re = 300$. The narrow domain was used in the computation for better resolution. Power spectral density plots of the velocity fluctuations at the same point as for figure 14 are shown in figure 15(*a–c*). The presence of a second period-doubling bifurcation can be detected, again more visible in the spanwise component w. The spectral densities following the second period-doubling bifurcation become considerably more wideband than at $Re = 300$. The phase-space plot (figure 16) in the (u, v, w)-space shows four limit cycles lying on different planes. The trajectory also seems to form 'cusp' points, indicative of a folded attractor.

For the computational domain considered here, the wake at $Re = 333$ is transitional. In order to reach the turbulent regime, the Reynolds number was subsequently increased to 500. The computation was continued for over twenty periods of oscillation (based on the Strouhal frequency). The power spectra of the u-, v- and w-velocity components are shown in figures 17(*a*), 17(*b*), and 17(*c*),

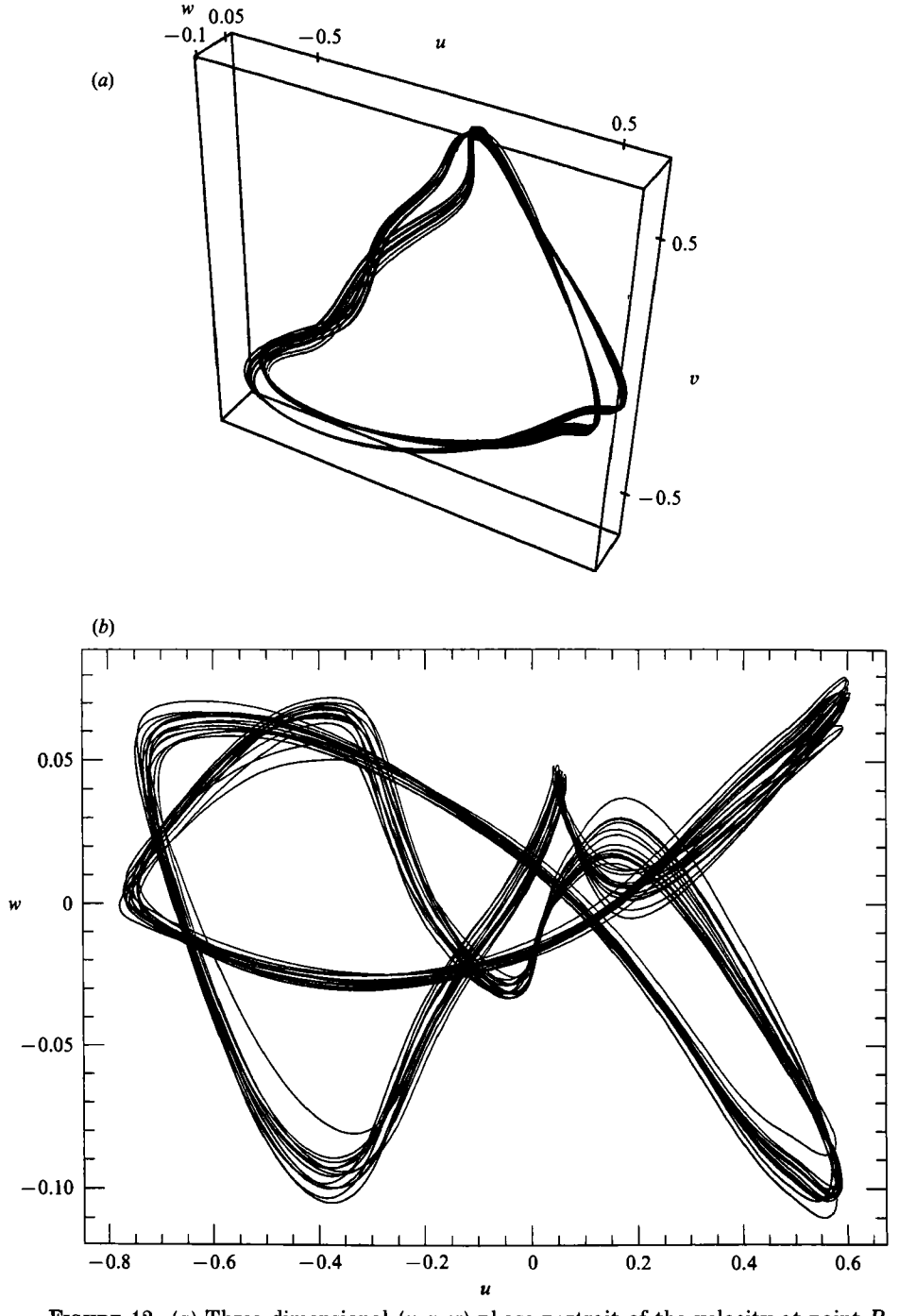

FIGURE 12. (*a*) Three-dimensional (u, v, w) phase portrait of the velocity at point P_1 and $Re = 300$. (*b*) Two-dimensional projection (u, w) of point P_1.

respectively. The w-component exhibits a wideband spectrum, with considerable low-frequency energy content. The v- and u-component spectra also show wideband form, with the Strouhal frequency prevailing. The spectra indicate that the flow is chaotic at this Reynolds number. (The fact that this flow state appears to lie at the

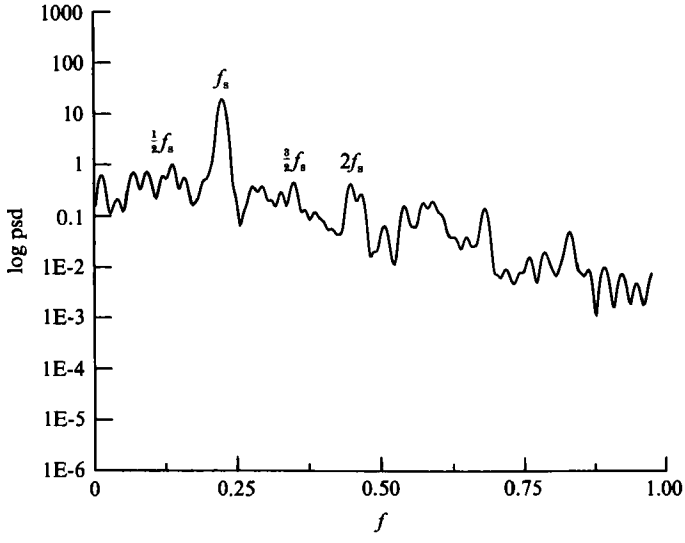

FIGURE 14. Power spectrum of w-component in a wide domain ($L_z = 2\pi$) at P_1 and $Re = 300$.

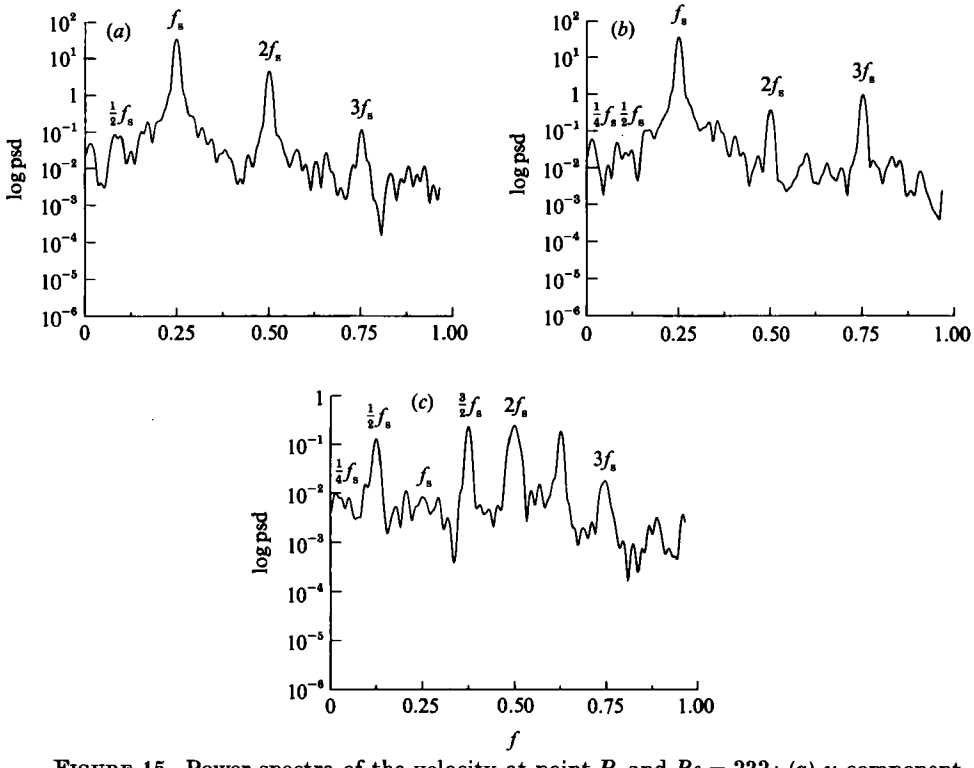

FIGURE 15. Power spectra of the velocity at point P_1 and $Re = 333$: (*a*) u-component, (*b*) v-component, (*c*) w-component.

'end' of a period-doubling cascade further supports this.) The strong presence of the Strouhal frequency in the spectra, lying well above the background noise, suggests that, despite the chaotic character of the flow, a coherent pattern (the three-dimensional vortex street, figure 18, plate 2) is still present, sustained by the absolute instability of the time-average flow.

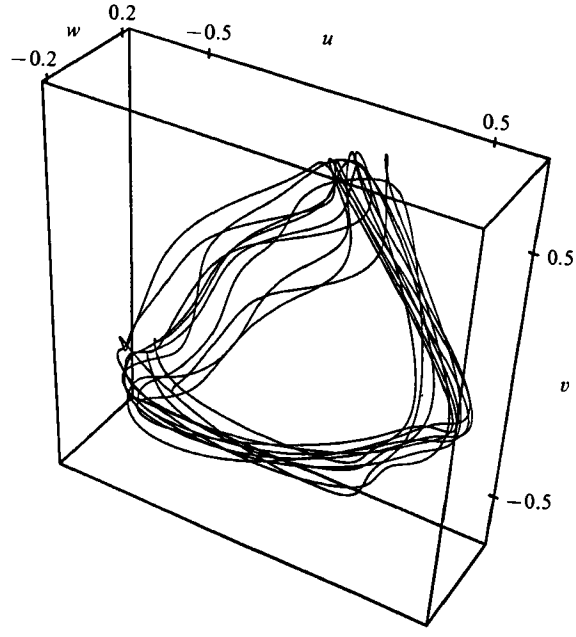

FIGURE 16. Three-dimensional phase portrait of velocity at P_1 and $Re = 333$.

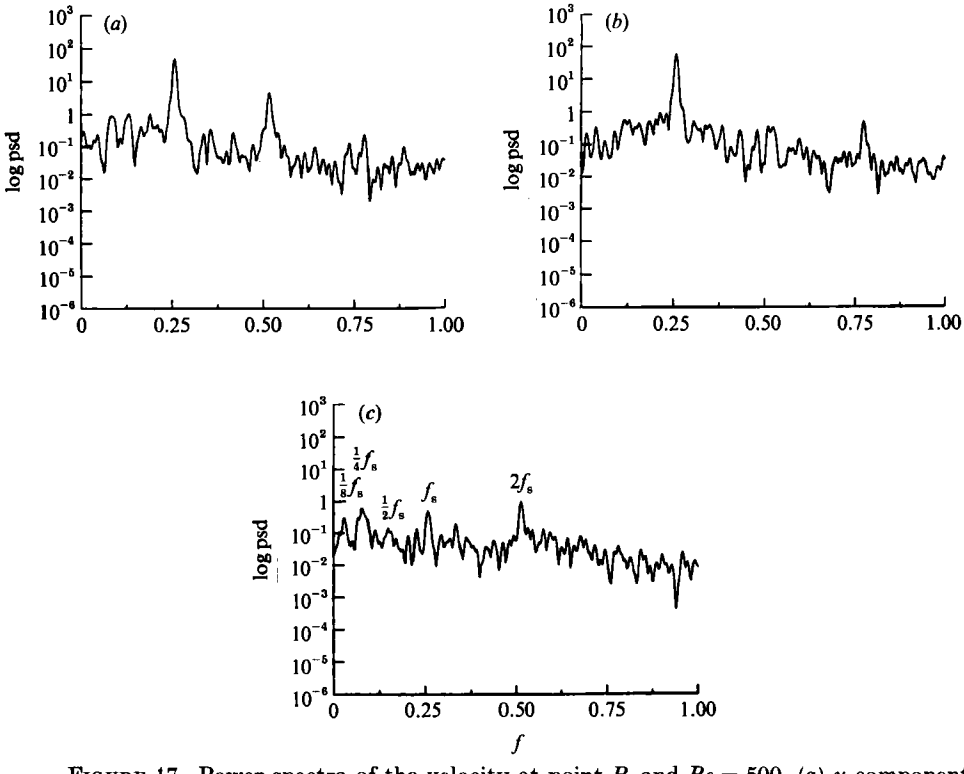

FIGURE 17. Power spectra of the velocity at point P_1 and $Re = 500$. (*a*) u-component, (*b*) v-component, (*c*) w-component.

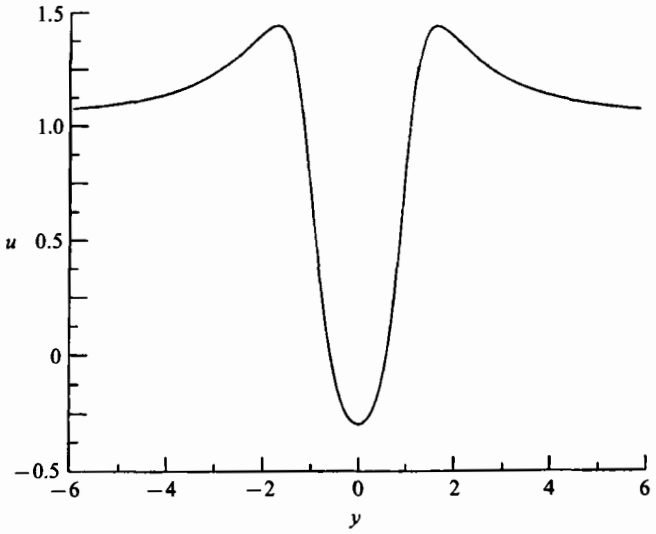

FIGURE 19. Streamwise time-average velocity profile at $x = 2.0$; $z = 1.0$ and $Re = 500$; a second inflexion point has been formed.

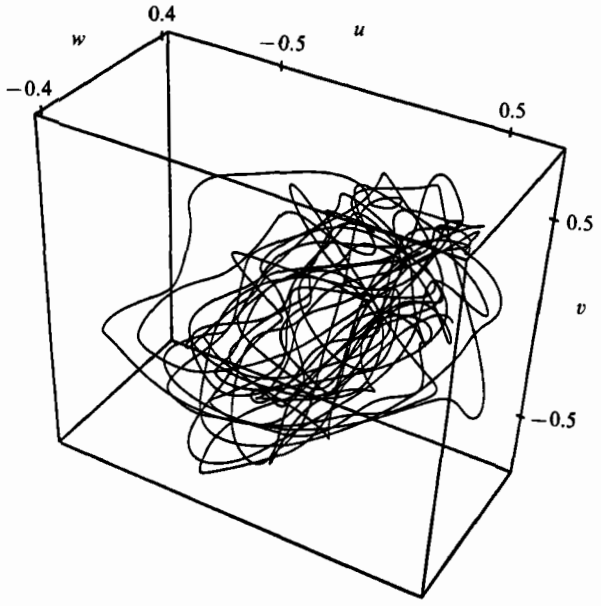

FIGURE 20. Three-dimensional phase portrait of velocity vector at P_1 and $Re = 500$.

The stability of the time-average flow in the near wake was analysed (location $x = 2, z = 1$). The plot of the time-average velocity at this location as a function of the coordinate y (figure 19) shows that a second inflexion point has been formed (verified by considering the first derivative of the profile), because of the growth of the separated shear layer. Despite the appearance of the second inflexion point, the Rayleigh equation for this flow has only one unstable mode, that associated with the vortex street as we verified numerically. Work in progress leads us to believe that the shear layer becomes unstable at a higher Reynolds number as the negative growth

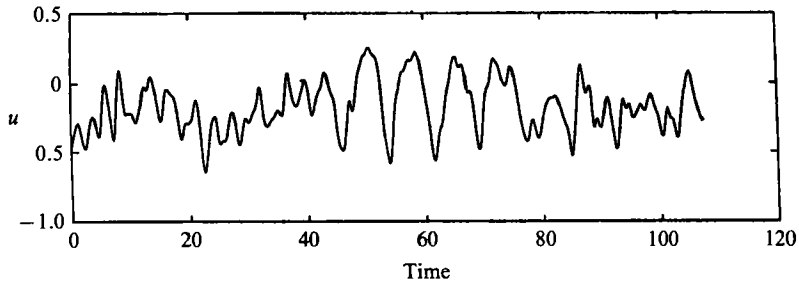

FIGURE 21. Time trace of streamwise velocity component at $x = 1.91$; $y = 0.12$) in the near wake; $Re = 500$.

rate at this Reynolds number tends to positive values as Reynolds number increases. (See also the experiments of Bloor 1964; Unal & Rockwell 1984.) The time-average flow is absolutely unstable, yielding a Strouhal number equal to 0.258, which agrees remarkably well with the value obtained from the numerical simulation ($St = 0.2596$). This underlines the significance of hydrodynamic instabilities of the time-average flow field in generating large-scale patterns in a chaotic flow. It provides further support for the results in Triantafyllou *et al.* (1986) (obtained from the analysis of experimental results at a much higher Reynolds number) that the absolute instability of wake flows persists in the turbulent regime too, and can account for the frequency of formation of the large-scale vortices.

The phase-space plot (figure 20) has an extremely tangled form; despite this complexity, the homoclinic trajectory corresponding to the first period doubling is still visible, suggesting that traces of the transition process still play some role in the dynamics of the chaotic flow. Intermittency and bursting phenomena were also observed at this Reynolds number. In figure 21 the time trace of the streamwise velocity component shows periods of almost periodic behaviour interspersed with periods of apparently random behaviour. It is clear therefore that the flow at this Reynolds number has some of the characteristics that are attributed to turbulence, namely the broadband spectra of the fluctuations and the presence of intermittency.

In order to characterize the flow as turbulent, however, the appearance of spatial chaos is also necessary. This, in general, requires the computation of particle paths, in order to demonstrate exponential divergence of fluid particles, as well as the computation of mean turbulence intensities over a long time period. In this paper the simpler, but less decisive, alternative of computing instantaneous streamlines has been followed. The spatial evolution of various instantaneous streamlines is shown in figure 22 (*a*, *b*) (plate 2): a complicated three-dimensional structure develops in the near wake, with substantial flow parallel to the axis of the cylinder. The streamlines in the spanwise direction are wavy, and twisted close to the ends of the domain (figure 22*a*); further downstream the streamlines have the typical structure of a three-dimensional vortex street (figures 22*b* and 18). The spatial structure of the flow at $Re = 500$ exhibits therefore the highest complexity of all cases considered in this paper. We cannot decisively conclude, however, whether the flow is turbulent or not; computation of particle trajectories and mean statistics will be required to finally resolve this issue.

6. Discussion

The main finding of the present work is that the route to chaos in the wake formed behind circular cylinders follows the general lines of Feigenbaum's (1978, 1979) period-doubling scenario. This is very encouraging for the applicability of this simple idea to flows in complex geometries, in a manner similar to that in 'simple flows' (as for example in Libchaber & Maurer 1982). In the present problem, the period-doubling process was found to originate in the near wake. This is based on the fact that power spectral densities downstream do not exhibit any subharmonics additional to those present in the near wake. The appearance of the period doubling can be attributed to the fact that two three-dimensional absolute instability modes are possible for the same time-average flow, and thus the flow alternates between them, doubling the time that is required to repeat itself.

A subject that deserves further attention is how closely the transition process follows Feigenbaum's theoretical scenario, which is one of the universal routes to chaos. In the present computation the one-half, one-quarter, and one-eighth components of fundamental frequency have been detected. A more detailed investigation seems currently a formidable task, requiring an enormous amount of computation, since extremely long time traces of the velocity fluctuations are required to reliably detect the presence of high-order subharmonics, and the magnitude of their spectral peaks. Thus Feigenbaum's (1978, 1979) scaling laws still await verification.

From the numerical experiments reported here it would appear that the period-doubling bifurcations in the wake are best seen in the spanwise velocity component. Thus, since only streamwise velocity components have been recorded in experiments, this might explain why the period-doubling cascade has remained undetected so far. Another possible reason is the difficulty of suppressing the three-dimensionality introduced by the end effects in Reynolds numbers over 200. End effects are in physical experiments unavoidable, and can induce three-dimensionality before the onset of the secondary instability. It is not clear whether end effects can suppress the period-doubling process, but it seems plausible that they can obscure its presence by introducing additional low-frequency spectral peaks (Williamson 1989; Konig, Eisenlohr & Eckelmann 1990). We note however that the 'low frequency fluctuations' observed by Bloor (1964), could be due to the period-doubling process.

The question of how the size of the computational domain as well as the resolution parameters influence the current findings is an important one. First, we have shown in table 1 that the size of the computational domain in the (x, y)-plane can alter the values of the Strouhal frequency; qualitatively, however, the vortex street retains its classical form and certainly there are no additional bifurcations introduced due to the relatively small domain size. The selection of the spanwise length L_z is also an important one: the spanwise structures visualized in the experiments of Hammache & Gharib (1989), and Williamson (1989) seem to extend over seven cylinder diameters. These structures, however, are caused by the presence of boundaries in the spanwise direction, and are not present in our computations, where the geometry is perfectly two-dimensional.

The computational tests performed in this work use two values of L_z (π and 2π), which correspond to a spanwise wavenumber of order one, around which the maximum growth of secondary instability is attained (Orszag & Patera 1983). We have found that our results as monitored in terms of time traces (and corresponding power spectra) as well as through flow visualization are the same for two of the

domains and $Re = 225$ and 300 where we carried out both computations. In particular, even the narrow domain allows the development of instantaneous flow structures that extend over two wavelengths in the span, while the corresponding time-average flow structures extend over four wavelengths (see figure 8). It is clear therefore that the wavelength in the spanwise structure is considerably smaller than the span of the domain L_z, and we can conclude that the computational results have not been seriously influenced by the choice of L_z.

As far as resolution requirements are concerned, computations with higher-order Legendre polynomials in (x, y)-planes as well as preliminary computations with a larger number of Fourier modes in the z-direction ($M = 32$, Tomboulides 1992), confirm the results reported in this paper. Moreover, recent work on the minimum spectral resolution requirements for simulating turbulence in channel flows (Zores 1989) has systematically documented that only four and six modes employed in the streamwise and spanwise directions respectively suffice in order to sustain turbulence fluctuations and predict the dynamics correctly in a much higher Reynolds number range ($Re > 3000$); the spectral resolution employed in the current simulations by far exceeds these requirements.

In summary, the behaviour of wake flows at Reynolds numbers in excess of 200 is inherently three-dimensional. In fact, the results of two-dimensional simulations at $Re = 500$ (figure 1) show such a striking difference with those of the three-dimensional simulation, and with experiments, that one has to wonder whether there is any point in performing two-dimensional simulations of wake flows after the onset of three-dimensionality. To quote Morkovin (1964), two-dimensional flows for all their computational and conceptual convenience seem to be part of a 'comfortable dream world'.

This work was supported by the Office of Naval Research under contracts N00014-91-J-1287, N00014-91-J-1373, and N00014-90-J-1315, National Science Foundation Grant CTS-8906911 and CTS-8906432, and National Oceanic and Atmospheric Administration Sea-Grant Contract NA86AA-D-SG089. Most computations were performed using the CRAY Y/MP Computer of the Pittsburgh Supercomputing Center, and at the Numerical Aerodynamic Simulation Facility at NASA Ames.

REFERENCES

Amon, C. H. & Patera, A. T. 1989 Numerical calculation of stable three-dimensional tertiary states in grooved-channel flow. *Phys. Fluids* A **1**, 2005–2009.

Arnol'd, V. I. 1972 Notes on the three-dimensional flow pattern of a perfect fluid in the presence of a small perturbation of the initial velocity field. *Appl. Math. Mech.* **36**, 236–242.

Batcho, P., Karniadakis, G. E. & Orszag, S. A. 1990 Numerical investigation of the spreading of self-excited stratified jets. *ASME Symp. on Non-Steady Fluid Mechanics, Toronto, Canada* (ed. J. Miller & D. P. Telionis), FED Vol. 92, pp. 487–495.

Bayly, B. J. 1986 Three-dimensional instability of elliptic flow. *Phys. Rev. Lett.* **57**, 2160–2163.

Bayly, B. J., Orszag, S. A. & Herbert, T. 1988 Instability mechanisms in shear-flow transition. *Ann. Rev. Fluid Mech.* **20**, 359–391.

Bers, A. 1983 Basic plasma physics I. In *Handbook of Plasma Physics* (ed. M. N. Rosenbluth & R. Z. Sagdeev), vol. 1, chap. 3.2. North Holland.

Bloor, S. M. 1964 The transition to turbulence in the wake of a circular cylinder *J. Fluid Mech.* **19**, 290–304.

Braza, M., Chassaing, P. & Ha Minh, H. 1986 Numerical study and physical analysis of the pressure and velocity fields in the near wake of a circular cylinder. *J. Fluid Mech.* **165**, 79–130.

CHEN, J. H., MANSOUR, N. N. & CANTWELL, B. J. 1989 Direct numerical simulation of transition in a compressible wake. *Seventh Symp. on Turbulent Shear Flows, Stanford, California* (ed. W. C. Reynolds *et al.*).

CHU, D., HENDERSON, R. & KARNIADAKIS, G. E. 1991 Parallel spectral element–Fourier simulation of turbulent flow over riblet-mounted surfaces. *Theor. Comp. Fluid Dynamics* (to appear).

DEANE, A. E., KEVREKIDIS, I. G., KARNIADAKIS, G. E. & ORSZAG, S. A. 1991 Low-dimensional models for complex geometry flows: Applications to grooved channels and circular cylinders. *Phys. Fluids* A **3**, 2337–2354.

DRAZIN, P. G. & REID, W. H. 1981 *Hydrodynamic Stability*. Cambridge University Press.

FEIGENBAUM, M. J. 1978 Quantitative universality for a class of nonlinear transformations. *J. Statist. Phys.* **19**, 25–52.

FEIGENBAUM, M. J. 1979 The onset spectrum of turbulence. *Phys. Lett.* **74A**, 375–377,

GOTTLIEB, D. & ORSZAG, S. A. 1977 *Numerical Analysis of Spectral Methods: Theory and Applications*. SIAM.

GRESHO, P. M., CHAN, R., UPSON, C. & LEE, R. 1984 A modified finite element method for solving the time-dependent, incompressible Navier–Stokes equations. Part 2. Applications. *Intl J. Numer. Meth. Fluids* **4**, 619–640.

HAMMACHE, M. & GHARIB, M. 1989 A novel method to promote parallel vortex shedding in the wake of circular cylinder. *Phys. Fluids* A **1**, 1611–1614.

HANNEMAN, K. & OERTEL, H. 1989 Numerical simulation of the absolutely and convectively unstable wake. *J. Fluid Mech.* **199**, 55–88.

HERBERT, T. 1988 Secondary instabilities of boundary layers. *Ann. Rev. Fluid Mech.* **20**, 487–526.

HORIUTI, K. 1987 Comparison of conservative and rotational forms in large eddy simulation of turbulent channel flow. *J. Comput. Phys.* **71**, 343–370.

KAIKTSIS, L., KARNIADAKIS, G. E. & ORSZAG, S. A. 1991 Onset of three-dimensionality, equilibria, and early transition in flow over a backward-facing step. *J. Fluid Mech.* **231**, 521–528.

KARNIADAKIS, G. E. 1989*a* Spectral element–Fourier methods for incompressible turbulent flows. *Proc. Intl Conf. on High-Order Numerical Methods, Como, Italy.*

KARNIADAKIS, G. E. 1989*b* Spectral element simulations of laminar and turbulent flows in complex geometries. *Appl. Numer. Maths* **6**, 85–105.

KARNIADAKIS, G. E. & AMON, C. 1987 Stability calculations of wall-bounded flows in complex geometries. In *Proc. Sixth IMACS Symp. on PDEs*, pp. 525–532.

KARNIADAKIS, G. E., BULLISTER, E. T. & PATERA, A. T. 1985 A spectral element method for solution of two- and three-dimensional time-dependent Navier–Stokes equations. In *Proc., Europe–US Conf. on Finite element Methods for Nonlinear Problems*, pp. 803–817. Springer.

KARNIADAKIS, G. E., ISRAELI, M. & ORSZAG, S. A. 1991*a* High-order splitting methods for incompressible Navier–Stokes equations. *J. Comput. Phys.* **97**, 414–443.

KARNIADAKIS, G. E., ORSZAG, S. A., RONQUIST, E. M. & PATERA, A. T. 1991*b* Spectral element and lattice gas methods for incompressible fluid dynamics. In *Incompressible Fluid Dynamics* (ed. M. D. Gunzburger & R. A. Nicolaides). Cambridge University Press.

KARNIADAKIS, G. E. & TRIANTAFYLLOU, G. S. 1989 Frequency selection and asymptotic states in laminar wakes. *J. Fluid Mech.* **199**, 441–469.

KARNIADAKIS, G. E. & TRIANTAFYLLOU, G. S. 1990 Direct numerical simulation of the three-dimensional vortex street. *AIAA*-90-0113.

KOCH, W. 1985 Local instability characteristics and frequency determination of self-excited wake flows. *J. Sound Vib.* **99**, 53.

KONIG, M., EISENLOHR, H. & ECKELMANN, H. 1990 The fine structure in the Strouhal–Reynolds number relationship of the laminar wake of a circular cylinder. *Phys. Fluids* A **2**, 1607–1614.

LASHERAS, J. C. & MEIBURG, E. 1990 Three-dimensional vorticity modes in the wake of a flat plate. *Phys. Fluids* A **2**, 371–380.

LIBCHABER, A. & MAURER, J. 1982 A Rayleigh–Bénard experiment: helium in a small box. In *Nonlinear Phenomena at Phase Transitions and Instabilities* (ed. T. Riste). NATO ASI Series B, vol. 77, p. 259.

MADAY, Y. & PATERA, A. T. 1989 Spectral element methods for the Navier–Stokes equations. In *State of the Art Surveys in Computational Mechanics*. ASME.

MEIBURG, E. & LASHERAS, J. C. 1988 Experimental and numerical investigation of the three-dimensional transition in plane wakes. *J. Fluid Mech.* **190**, 1–37.

METCALFE, R. W., ORSZAG, S. A., BRACHET, M. I., MENON, S. & RILEY, J. J. 1987 Secondary instability of a temporally growing mixing layer. *J. Fluid Mech.* **184**, 207–243.

MONKEWITZ, P. A. & NGUYEN, L. 1987 Absolute instability in the near wake of two-dimensional bluff bodies. *J. Fluids Struct.* **1**, 165–182.

MORKOVIN, M. V. 1964 Flow around circular cylinders. A kaleidoscope of challenging fluid phenomena. *ASME Symp. on Fully Separated Flows, Philadelphia*, p. 102.

ORSZAG, S. A. & PATERA, A. T. 1983 Secondary instability of wall-bounded shear flows. *J. Fluid Mech.* **128**, 347–385.

PATERA, A. T. 1984 A spectral element method for fluid dynamics; laminar flow in a channel expansion. *J. Comput. Phys.* **54**, 468–488.

PIERREHUMBERT, R. T. 1986 Universal short-wave instability of two-dimensional eddies in an inviscid fluid. *Phys. Rev. Lett.* **57**, 2157–2159.

PIERREHUMBERT, R. T. & WIDNALL, S. E. 1982 The two- and three-dimensional instabilities of a spatially period shear layer. *J. Fluid Mech.* **114**, 59–82.

RONQUIST, E. M. 1988 Optimal spectral element methods for the unsteady three-dimensional incompressible Navier–Stokes equations. Ph.D. thesis, MIT. Cambridge, Massachusetts.

SQUIRE, H. B. 1933 On the stability for three-dimensional disturbances of viscous fluid flow between parallel walls. *Proc. R. Soc. Lond.* A **142**, 621–628.

STRYKOWSKI, P. J. & SREENIVASAN, K. R. 1990 On the formation and suppression of vortex 'shedding' at low Reynolds numbers. *J. Fluid Mech.* **218**, 71–107.

TOMBOULIDES, A. G. 1992 Direct and large eddy simulation of wake flows. Ph.D. thesis, Princeton University, Princeton, New Jersey.

TOMBOULIDES, A. G., ISRAELI, M. & KARNIADAKIS, G. E. 1989 Efficient removal of boundary-divergence errors in time splitting methods. *J. Sci. Comput.* **4**, 291–308.

TOMBOULIDES, A. G., ISRAELI, M. & KARNIADAKIS, G. E. 1991 Viscous-sponge outflow boundary condition for incompressible flows. *Mini-symposium on Outflow Boundary Conditions, Stanford, August*, 1991.

TRIANTAFYLLOU, G. S. 1990 Three-dimensional flow patterns in two-dimensional wakes. *ASME Symp. on Non-Steady Fluid Mechanics, Toronto, Canada* (ed. J. Miller & D. P. Telionis), FED Vol. 92, pp. 395–402.

TRIANTAFYLLOU, G. S. & KARNIADAKIS, G. E. 1990 Computational reducibility of unsteady viscous flows. *Phys. Fluids* A **2**, 653–656.

TRIANTAFYLLOU, G. S., TRIANTAFYLLOU, M. S. & CHRYSSOSTOMIDIS, C. 1986 On the formation of vortex streets behind stationary cylinders. *J. Fluid Mech.* **177**, 461–477.

UNAL, M. F. & ROCKWELL, D. 1984 The role of shear layer stability on vortex shedding from cylinders. *Phys. Fluids* **27**, 2598–2599.

UNAL, M. F. & ROCKWELL, D. 1988 On vortex formation from a cylinder. Part 1. The initial instability. *J. Fluid Mech.* **190**, 491–512.

WILLIAMSON, C. H. K. 1988 The existence of two stages in the transition to three-dimensionality of a cylinder wake. *Phys. Fluids* **31**, 3165–3168.

WILLIAMSON, C. H. K. 1989 Oblique and parallel modes of vortex shedding in the wake of a circular cylinder at low Reynolds numbers. *J. Fluid Mech.* **206**, 579–627.

ZORES, R. 1989 Numerische untersuchungen mit einem grobauflosenden simulations modell fur die turbulente Kanalstromung. *Tech. Rep.* IB 221-89 A 24. Institut fur Theoretische Stromungsmechanik, DLR, Gottingen.